Title

Allele-specific dysregulation of lipid and energy metabolism in early-stage hypertrophic cardiomyopathy

Authors

Vaniya, Arpana

Karlstaedt, Anja

Gulkok, Damla

et al.

Publication Date

2024-06-01

DOI

10.1016/j.jmccpl.2024.100073

Peer reviewed

Journal of Molecular and Cellular Cardiology Plus 8 (2024) 100073

Contents lists available at ScienceDirect

Journal of Molecular and Cellular Cardiology Plus

journal homepage: www.journals.elsevier.com/journal-of-molecular-andcellular-cardiology-plus

Allele-specific dysregulation of lipid and energy metabolism in early-stage hypertrophic cardiomyopathy

Arpana Vaniya [a,1], Anja Karlstaedt [b,c,1], Damla Gulkok [d], Tilo Thottakara [d], Yamin Liu [d], Sili Fan [a], Hannah Eades [d], Styliani Vakrou [d], Ryuya Fukunaga [e], Hilary J. Vernon [f,g], Oliver Fiehn [a,*], M. Roselle Abraham [d,*]

[a] West Coast Metabolomics Center, University of California, Davis, Davis, CA, United States of America
[b] Department of Cardiology, Smidt Heart Institute, Cedars-Sinai Medical Center, Los Angeles, CA, United States of America
[c] Department of Biomedical Sciences, Cedars-Sinai Medical Center, Los Angeles, CA, United States of America
[d] Hypertrophic Cardiomyopathy Center of Excellence, Division of Cardiology, University of California San Francisco, San Francisco, CA, United States of America
[e] Department of Biological Chemistry, Johns Hopkins University, Baltimore, MD, United States of America
[f] McKusick Nathans Department of Genetic Medicine, Johns Hopkins University, Baltimore, MD, United States of America
[g] Department of Pediatrics, Johns Hopkins University, Baltimore, MD, United States of America

ARTICLE INFO

Keywords:
Untargeted metabolomics
Lipidomics
Hypertrophic cardiomyopathy
RNAseq
HCM mouse models

ABSTRACT

Introduction: Hypertrophic cardiomyopathy (HCM) results from pathogenic variants in sarcomeric protein genes that increase myocyte energy demand and lead to cardiac hypertrophy. However, it is unknown whether a common metabolic trait underlies cardiac phenotype at the early disease stage. To address this question and define cardiac biochemical pathology in early-stage HCM, we studied two HCM mouse models that express pathogenic variants in cardiac troponin T (*Tnt2*) or myosin heavy chain (*Myh6*) genes, and have marked differences in cardiac imaging phenotype, mitochondrial function at early disease stage.

Methods: We used a combination of echocardiography, transcriptomics, mass spectrometry-based untargeted metabolomics (GC-TOF, HILIC, CSH-QTOF), and computational modeling (CardioNet) to examine cardiac structural and metabolic remodeling at early disease stage (5 weeks of age) in R92W-TnT$^{+/-}$ and R403Q-MyHC$^{+/-}$ mutant mice. Data from mutants was compared with respective littermate controls (WT).

Results: Allele-specific differences in cardiac phenotype, gene expression and metabolites were observed at early disease stage. LV diastolic dysfunction was prominent in TnT mutants. Differentially-expressed genes in TnT mutant hearts were predominantly enriched in the Krebs cycle, respiratory electron transport, and branched-chain amino acid metabolism, whereas MyHC mutants were enriched in mitochondrial biogenesis, calcium homeostasis, and liver-X-receptor signaling. Both mutant hearts demonstrated significant alterations in levels of purine nucleosides, trisaccharides, dicarboxylic acids, acylcarnitines, phosphatidylethanolamines, phosphatidylinositols, ceramides and triglycerides; 40.4 % of lipids and 24.7 % of metabolites were significantly different in TnT mutants, whereas 10.4 % of lipids and 5.8 % of metabolites were significantly different in MyHC mutants. Both mutant hearts had a lower abundance of unsaturated long-chain acyl-carnitines (18:1, 18:2, 20:1), but only TnT mutants showed enrichment of FA18:0 in ceramide and cardiolipin species. CardioNet predicted impaired energy substrate metabolism and greater phospholipid remodeling in TnT mutants than in MyHC mutants.

Conclusions: Our systems biology approach revealed marked differences in metabolic remodeling in R92W-TnT and R403Q-MyHC mutant hearts, with TnT mutants showing greater derangements than MyHC mutants, at early disease stage. Changes in cardiolipin composition in TnT mutants could contribute to impairment of energy metabolism and diastolic dysfunction observed in this study, and predispose to energetic stress, ventricular arrhythmias under high workloads such as exercise.

* Corresponding authors.
E-mail addresses: ofiehn@ucdavis.edu (O. Fiehn), Roselle.Abraham@ucsf.edu (M.R. Abraham).
[1] Contributed equally.

https://doi.org/10.1016/j.jmccpl.2024.100073
Received 15 February 2024; Received in revised form 21 March 2024; Accepted 28 March 2024
Available online 31 March 2024

1. Introduction

Hypertrophic cardiomyopathy (HCM), the most common cardiac genetic disease worldwide [1], is characterized by myocyte hypertrophy, fibrosis, left ventricular (LV) hypercontractility [2], diastolic dysfunction [3], and diverse clinical outcomes, ranging from asymptomatic to heart failure and sudden death [4]. HCM stems from pathogenic variants in sarcomeric protein genes that induce changes in myofilament calcium sensitivity [5–7], cross-bridge kinetics [8–10], cardiac mechanics [3,11] signaling pathways [12] and gene expression [13,14]. The incorporation of mutant proteins in sarcomeres has been demonstrated to increase the energy cost of tension generation [15], and induce energetic stress [15,16], which has led to the notion that HCM is a metabolic disease [16–18].

Metabolic adaptation and structural remodeling in the heart are functionally linked [18–20]. Cardiac hypertrophy is associated with metabolic alterations that promote changes in gene expression. Furthermore, intermediary metabolites in the heart serve as signals to initiate and sustain cardiac adaptation to stress [21]. Hence, understanding metabolic alterations induced by pathogenic variants of sarcomeric protein genes may advance the design of metabolism-based therapies [22], preventing the development and progression of HCM.

Recent advances in untargeted mass spectrometry-based metabolomics have expanded our understanding of the mechanistic links between metabolism and the development and progression of human diseases [23–26]. Studies in HCM patients at established disease stages have demonstrated *genotype-independent* mitochondrial dysfunction and broad metabolic/lipid remodeling in heart tissue [27–29]. However transcriptomic and functional studies in two mouse models (R92W-TnT$^{+/-}$, R403Q-MyHC$^{+/-}$) at early disease stage revealed *genotype-specific* changes in the expression of metabolic genes, mitochondrial function, and cellular redox state [13]. It is currently unknown whether a common metabolic trait is present in HCM hearts, at the early-disease stage. To address this question and define the underlying biochemical pathology in early-stage HCM, we conducted cardiac phenotyping by echocardiography, in-depth untargeted mass spectrometry (MS)-based metabolomics and lipidomics analysis followed by pathway and network analysis, and mathematical modeling [30] in R92W-TnT [9,31] and R403Q-MyHC [32] mouse hearts [13,14] that express pathogenic variants in two different sarcomeric protein genes, namely cardiac troponin T (*Tnnt2*) or α-Myosin Heavy Chain (*Myh6*) [32] gene. These mouse models are based on families with clinical phenotypes that span the spectrum of human disease, namely mild or no clinical left ventricular hypertrophy (LVH), sudden death at a young age [33] in R92W-TnT$^{+/-}$, and moderate LVH with heart failure requiring transplantation in middle age [34,35] in R403-βMyHC$^{+/-}$. Residue 92 is located in the αlpha-tropomyosin-binding domain of cardiac troponin T, whereas residue 403 is located in the actin-binding motor domain of myosin heavy chain [36]. Both mutant proteins are incorporated into sarcomeres [9,37] and increase tension cost [15,34,38] but have markedly different biophysical effects [39]. R92W-TnT$^{+/-}$ confers increased myofilament Ca^{2+} sensitivity of force development [9] and is associated with LV hypercontractility, diastolic dysfunction, reduction of ventricular mass [9], interstitial fibrosis, and induction of the fetal gene program [9]. R92W-TnT$^{+/-}$ myocytes exhibit shorter baseline sarcomere lengths, higher resting intracellular Ca^{2+} levels as well as a reduction in the amplitude, rate of rise and fall of cytoplasmic Ca^{2+} transients [40], without a change in tension-dependent ATP consumption [41]. Studies in R403Q-MyHC$^{+/-}$ show reduced myofibrillar contractility [42,43], greater myofiber isometric tension development at submaximal Ca^{2+} levels [44], and slower LV relaxation [45]. Heterozygous expression of R403Q-MyHC in mice leads to progressive LVH, left atrial enlargement, reduced fractional shortening, cardiac fibrosis, and LV dilation [32,46].

In this study, we discovered allele-specific cardiac structural, metabolic, and lipidomic remodeling, as well as differences in lipid peroxidation, substrate utilization, and energy provision, which could underlie differences in cardiac HCM phenotype at early disease stage.

2. Methods

All procedures involving the handling of animals were approved by the Animal Care and Use Committee of the University of San Francisco California (UCSF) and adhered to NIH Public Health Service guidelines.

2.1. Transgenic mouse models

The R92W-TnT$^{+/-}$ male mouse breeders were kindly provided by Dr. Jill Tardiff (University of Arizona), and the R403Q-αMyHC$^{+/-}$ male mouse breeders were kindly provided by Dr. Leslie Leinwand (University of Colorado Boulder). The R92W-TnT mouse is an F1 cross between FVB/N and C57/Bl6 strains [9,47], and the R403Q-αMyHC mice were generated in CBA/B16 (F1 cross) mice [32]. The R92W-TnT$^{+/-}$ and R403Q-MyHC$^{+/-}$ mice were backcrossed to C57BL/6 N (Charles River) for >10 generations. Male mice were weaned and genotyped at 4 weeks by PCR-amplified tail DNA as described previously [13]. All studies were conducted at five weeks of age.

2.2. Mouse phenotyping by echocardiography

Cardiac phenotyping was performed by echocardiography using a Vevo 3100 platform and MX550D 40Mhz probe (VisualSonics, Toronto, Canada). Five-week-old R92W-TnT and R403Q-MyHC mice and littermate controls (WT) were anesthetized using inhaled isoflurane (3 *v*/v% for induction and 0.5–1 % v/v% for maintenance). Parasternal long (PLSAX) images were recorded in B-mode and M-mode. To evaluate diastolic function, pulsed-wave (PW) Doppler of mitral valve (MV) inflow, tissue Doppler imaging, and left atrial (LA) area were recorded using the apical 4-chamber view. Pulsed-wave Doppler of pulmonary wave flow in the PSLAX view was used to measure pulmonary acceleration time (PAT), which reflects mean pulmonary artery pressure; PAT was indexed to RR interval to account for variability in mouse heart rate under anesthesia. Heart rate was >450 bpm during recording of systolic parameters [48] and >400 bpm during recording of parameters reflecting diastolic function. Data was analyzed using the Vevo Image Lab Software (Version 5.6.0, VisualSonics, Toronto, Canada). Echocardiographic measurements were averaged from at least 3 separate cardiac cycles. Statistical Analysis was carried out using R (version 4.1.0) using the package gtsummary (version 1.4.1).

2.3. Metabolomics

2.3.1. Sample preparation

Mice were euthanized by cervical dislocation, between 12 PM and 2 PM, following which the heart was rapidly excised, washed in ice cold PBS, flash frozen in liquid nitrogen (within 30 s of opening the chest), and stored at −80 °C until processing for metabolomics. Whole hearts were first homogenized in 100 μL ACN using 4–3 mm stainless steel grinding balls for 30 s at a time for two rounds at 15,000 rotations per minute (rpm). Homogenized hearts were lyophilized overnight until a dry powder was obtained. Extraction for the lipidomics analysis was carried out using the Matyash et al. protocol [49]. Ice-cold (975 μL) of 3:10 (*v*/v) MeOH/MTBE with QC mix containing 19 internal standards was added to 5 mg of freeze-dried samples. Samples were mixed for 10 s and then shaken for 5 min at 4 °C; 188 μL of LC-MS grade H_2O was added, mixed for 20 s, and centrifuged for 2 min at 14,000 relative centrifugal force (rcf); 350 μL of the upper organic phase was separated into two new tubes; 100 μL from each sample analysis tube was transferred to a new tube to create a pooled sample. Samples were dried down and re-suspended with 110 μL of 9:1 (*v*/v) MeOH:Tol with 50 ng/mL CUDA before analysis; 50 μL was aliquoted into two separate amber glass vials with microvolume inserts for an injection in each mode. For HILIC analysis, 120 μL of the bottom aqueous phase from the lipidomics

extraction mentioned above was split into two tubes. Samples were dried down and re-suspended in 100 µL of 80:20 (*v*/v) ACN:H_2O with internal standards. The resuspension solvent for HILIC contains 42 internal standards. Samples were then mixed for 10 s, sonicated for 5 min, and centrifuged for 2 min at 16,100 rcf. 90 µL was aliquoted into glass amber vials with microinserts prior to injection. For GC-TOF analysis, extraction and derivatization were carried out using the methods described in Fiehn et al. [23–25]. One milliliter of degassed, −20 °C pre-chilled extraction solvent of 3:3:2 (*v*/v/v) ACN:IPA:H_2O was added to 4 mg of freeze-dried sample. Samples were mixed for 10 s, shaken for 5 min at 4 °C, and then centrifuged for 2 min at 14,000 rcf. Two aliquots of 475 µL of the supernatant were separated into two tubes; 500 µL of 50:50 (*v*/v) ACN:H_2O was added to dried-down samples to clean up excess proteins, then mixed for 10 s and centrifuged for 2 min at 14,000 rcf; 475 µL of the supernatant was transferred to a new 1.5 mL tube which was then dried down to complete dryness. For derivatization, 10 µL MeOX solution was added to the sample and shaken for 1.5 h at 30 °C. For trimethylsilylation, 91 µL of MSTFA with FAMEs internal standards mixture was added to each sample. Samples were centrifuged for 2 min at 14,000 rcf, transferred to a GC crimp top glass vial with microvolume inserts, and immediately capped with GC vial crimp caps for analysis.

2.3.2. Reagents

Water (H_2O) (Optima LC/MS grade), methanol (MeOH) (Optima LC/MS grade), acetonitrile (ACN) (Optima LC/MS grade), 2-propanol (IPA) (Optima LC/MS grade), chloroform ($CHCl_3$) (HPLC grade), hexane (Certified ACS), ammonium acetate (AA), methyl tert-butyl ether (MTBE), toluene (Tol) (HPLC grade 99.9 %), formic acid (FA), ammonium formate (AmFo), Val-Tyr-Val, methoxyamine hydrochloride (MeOX), *N*-methyl-N-(trimethylsilyl)-trifluoroactamide (MSTFA), and pyridine (Anhydrous, 99.8 %) were all purchased from Fisher Scientific (Hampton, NH, USA). Fatty acid methyl esters (FAMEs) are a mixture made from 13 standards purchased from Fisher Scientific and Sigma-Aldrich. 12-(cyclohexylcarbamoylamino)-dodecanoic acid (CUDA) was purchased from Cayman Chemical Company (Ann Arbor, MI, USA). Internal standards for the quality control (QC) mix for the lipidomics extraction were purchased from Nu-Check Prep, Inc. (Elysian, MN, USA), Avanti Polar Lipids (Alabaster, AL, USA), CDN Isotopes (Quebec, Canada), and Sigma-Aldrich. The internal standards in the resuspension solvent for HILIC analysis were purchased from CDN Isotopes, Cayman Chemicals (Ann Arbor, MI USA), Sigma-Aldrich, Toronto Research Chemicals, Inc. (Ontario, Canada), and Cambridge Isotope Laboratories, Inc. CIL Cambridge (Tewksbury, MA, USA).

2.4. Instrumentation and metabolomic profiling

2.4.1. LC-MS/MS analysis (lipidomics and HILIC analysis)

Complex lipids were separated on a Waters Acquity UPLC CSH C18 column (100 × 2.1 mm; 1.7 µm) coupled to a Waters Acquity UPLC CSH C18 VanGuard pre-column (5 × 2.1 mm; 1.7 µm). The column was maintained at 65 °C with a 0.6 mL/min flow rate. The positive ionization mobile phases consisted of (A) 60:40 (*v*/v) ACN:H_2O with 10 mM ammonium formate and 0.1 % formic acid and (B) 90:10 (v/v) IPA/ACN with 10 mM ammonium formate and 0.1 % formic acid. For negative mode, 10 mM ammonium acetate was used as the modifier. The following gradient was used: 0 min 15 % B; 0-2 min 30 % B; 2–2.5 min 48 % B; 2.5–11 min 82 % B; 11–11.5 min 99 % B; 11.5–12 min 99 % B; 12–12.1 min 15 % B; 12.1–15 min 15 % B. 0.5 µL (ESI+) and 5.0 µL (ESI-) of the sample were injected. The Agilent 6530 Q-TOF mass spectrometer (MS) coupled to an Agilent 1290 Infinity ultra-high-performance liquid chromatography (UHPLC) was operated in both positive and negative electrospray ionization (ESI) mode. Full MS1 data was acquired on pooled samples. The following parameters for Full MS1 were used: mass range *m/z* 120–1700 (ESI+) and *m/z* 60–1700 (ESI-), gas temperature 325 °C, drying gas (nitrogen) flow rate 8 L/min, nebulizer 35 psig, sheath gas (nitrogen) flow rate 11 L/min, sheath gas temperature 350 °C, VCap 3500 V, and nozzle voltage 1000 V. AutoMS/MS is acquired using the following parameters: mass ranges using Static Exclusion Range list *m/z* 120–700, *m/z* 700–800, *m/z* 800–880, and *m/z* 880–1700 (ESI+) and *m/z* 60–700, *m/z* 700–800, *m/z* 800–880, and *m/z* 880–1700 (ESI-). *Use Formula* option was applied to ramp collision energies (CE) from low to high. The following parameters were used: slope 3 (ESI+) and 4 (ESI-), Offset 2.5 (ESI+/−), and charge All (ESI +/−). Data were acquired in centroid.

Biogenic amines were analyzed by HILIC LC-MS/MS analysis. Metabolites were separated on a Waters Acquity UPLC BEH Amide column (150 × 2.1 mm; 1.7 µm) coupled to an Acquity UPLC BEH Amide VanGuard pre-column (5 × 2.1 mm; 1.7 µm). The column was maintained at 40 °C with a 0.4 mL/min flow rate. The mobile phase consisted of (A) H_2O with 10 mM ammonium formate and 0.125 % formic acid at pH 3 and (B) 95:5 (*v*/v) ACN/H_2O with 10 mM ammonium formate and 0.125 % formic acid at pH 3. The following gradient was used: 0 min 100 % B; 0–2 min 100 % B; 2–7 min 70 % B; 7–7.9 min 40 % B; 9.5–10.25 min 30 % B; 10.25–12.75 min 100 % B; 16.75 min 100 % B. 1.0 µL (ESI+) of the sample was injected. The SCIEX 6600 TripleTOF MS coupled to an Agilent 1290 Infinity UHPLC was operated in positive ESI mode using the following parameters: mass range 50–1500 Da (MS1) and 40–1000 Da (MS/MS using Information Acquistion), 35 CE V, Duration 13.999 min, Cycle Time 0.5002 s, and Accumulation Time 0.250017 s. The following source parameters with arbitrary units were used: curtain gas (CUR) 35, IonSpray Voltage (IS) 4000, temperature (TEM) 500, Ion Source Gas (GSI) 50, and Ion Source Gas 2 (GS2). Data was acquired in centroid.

2.4.2. GC–MS analysis (primary metabolism by GC-TOF)

Data for primary metabolites was acquired on the LECO Pegasus High-Throughput TOF-MS coupled to an Agilent 7890 A gas chromatograph with Gerstel MultiPurpose Autosampler. Separation was achieved on Restek RTX-5Sil MS column (30 m length, 0.25 mm i.d., and 0.25 µm 95 % dimethyl 5 % diphenyl polysiloxane film) with a 10 m guard column. The injection volume was 0.5 µL at 250 °C. The GC used the flowing oven program held for 1 min at 50 °C, ramped to 330 °C at 20 °C/min, and held for 5 min before cool-down. The transfer line temperature was 280 °C. Spectra were recorded with the following parameters: mass range 85–500 u, electron ionization (EI) mode 70 eV, filament temperature 250 °C, acquisition time 20 min, and scan rate 17 spectra/s.

2.5. Data processing

2.5.1. LC-MS/MS

Untargeted LC-MS/MS data was analyzed by MS-DIAL software version 3.52 for lipidomics and 3.06 for HILIC [26]. Detailed parameter settings for lipidomics and HILIC data processing are listed in Supplemental Table 1. Metabolite annotations were done using our in-house developed mass-to-charge-retention time (*m/z*-RT) libraries. MS/MS spectral matching was performed using freely available MS/MS libraries obtained from www.massbank.usthe Mass Bank of North America (MoNA) (www.massbank.us) and the NIST17 MS/MS library.

2.5.2. GC–MS

The peak and compound detection or deconvolution was performed with the LECO ChromaTOF software version 4.50.1. Spectra were matched against the FiehnLib mass spectral and retention index library [50]. Post-curation and peak replacements were performed with the in-house developed BinBase software [51], and the sample matrix with all known and unknown compounds was exported to a Microsoft EXCEL sheet. Peak heights were normalized by mTIC normalization; mTIC is defined as the sum of all the peak heights for all identified metabolites.

2.6. Mathematical modeling of HCM heart metabolism

In silico simulations were performed using the metabolic network of the cardiomyocyte, CardioNet [30,52,53]. Mathematical modeling has previously been used to study the dynamics of cardiac metabolism in response to stress [30,54,55], and CardioNet has been successfully applied to identify limiting metabolic processes and estimate flux distributions [52,55]. Flux balance analysis (FBA) allows estimating flux rates in a cellular model based on metabolic constraints that are defined by the extracellular environment (e.g., oxygen and nutrient supply), cellular demands (e.g., proliferation, contraction) and tissue type. This modeling approach combines biochemical network models with optimality problems, which describe different cost or benefit functions and allow us to include experimental data, for example, metabolite levels, enzyme levels, or flux rates. The advantage of flux balance analysis is that it considers the system-wide effects of processes and allows us to assess metabolic limitations in an unbiased approach. We applied flux balance analysis to identify which reactions are involved in myocardial metabolic adaptations to R92W-TnT or R403Q-MyHC variants. Metabolic flux distributions were calculated using constrained-based modeling. To calculate flux rate changes (v_i), we constrained the model for each metabolite using experimentally determined metabolite concentrations (^{1}H NMR) to maximize cardiac work reflected by ATP hydrolysis (v_{ATPase}). Simulations were run with boundary conditions reflecting the circulating metabolite composition based on previously reported values and common metabolites in plasma [56–59]. Based on these constraints, we first determined flux distributions (v_m) under sham operation (control) conditions. We then calculated fold-changes (FC) for experimentally-measured metabolite concentrations between control and R92W-TnT or R403Q-MyHC and used these fold-changes to constrain fluxes further (v_m) for the synthesis and degradation of intracellular metabolites. We included fold-changes (FC) based on the assumption that changes in metabolite concentrations under experimental conditions are accompanied by a proportional increase or decrease in the respective flux for the metabolite pool. Using metabolite level changes (fold changes) to estimate flux rate changes (v_{FC}), we imply that the altered steady-state concentrations of metabolites are reflected in the newly evolved flux state and potentially limit metabolic functions. The following flux balance analysis was applied to identify steady-state flux distributions that agree with applied substrate uptake and release rates and changes in metabolite pools:

$$max v_{ATPase}$$

subject to

$$S \bullet v = 0,$$

$$v_i^{(-)} \le v_i \le v_i^{(+)},$$

$$L_j^{(-)} \le v_j \le L_j^{(+)} \ (j = j_1, j_2, \ldots),$$

$$v_m \le FC_m \bullet v_m^0 \ (m = m_1, m_2, \ldots),$$

where v_i denotes the flux rate change through the reaction i, v_j denotes the measured uptake or secretion rate through reaction j, S is the stoichiometric matrix, and $v_i^{(-)}$ and $v_i^{(\mp)}$ are flux constraints. The GUROBI LP solver was used to find the solution to the FBA problems. [60] The logarithm of the metabolic flux rate values is presented as heatmaps. Metabolic reactions are clustered according to their association to metabolic pathways, and plot colors indicate estimated flux rates for each metabolic reaction. All reactions and their metabolic subsystems are classified in the Kyoto Encyclopedia of Genes and Genomes database [61].

2.7. Statistical analysis

The Wilcox rank sum exact test was used to compare echocardiography data of mutants with littermate controls (WT). The Mann-Whitney U test was used to compared mutants with respective littermate controls (TnT vs WT, MyHC vs WT). The fold change of each comparison was calculated as the group median ratio. To control the false discovery rate (FDR), we adopted the Benjamini-Hochberg FDR correction procedure [62]. We performed chemical enrichment analysis (ChemRICH) [63] using the p-values and fold changes to access chemical classes significantly altered ($p < 0.05$) in each comparison. ChemRICH provides enrichment analysis based upon chemical structure and not pre-defined pathways which can be inherently flawed and does not rely upon background databases for statistical calculations. Metabolite cluster significance was calculated using Kolmogorov–Smirnov test. Metabolites were considered significant using the Mann-Whitney U test if $p < 0.05$. Downstream analysis of processed metabolomics data relied on (1) the use of non-parametric statistical methods, which do not make assumptions on the underlying distribution of the data, and (2) the use of littermate control mouse heart tissue as a “control” or “reference” metabolome by which to identify specific metabolic changes due pathogenic variants in sarcomeric protein genes. We annotated metabolites to identifiers of several key databases including KEGG, HMDB, PubChem IDs and CardioNet [30].

3. Results

3.1. Heterozygous expression of pathogenic variants in Tnnt2 and Myh6 promote gene expression changes at early disease stage

We used two well characterized murine models of HCM, R92W-TnT and R403Q-αMyHC [8,9,13,14,31,64–66] (Fig. 1A and B) to define the metabolic phenotype in HCM hearts, at early disease stage (5 weeks of age). The mutant TnT transgene construct [47] is composed of a nucleotide change that results in the substitution of a single amino acid (R-> W) at codon 92, along with a myc tag at the N-terminus in murine cTnT, and the mutant MyHC transgene construct consists of a point mutation along with a deletion of 59 amino acids in the actin-binding domain of αMHC bridged by 9 non-myosin amino acids [65]. Using echocardiography, we observed significantly lower left ventricle (LV) mass and smaller LV cavity size in mutant TnT hearts, and a trend towards higher LV mass in mutant MyHC hearts, when compared to respective littermate controls (WT) (Fig. 1C, Supplemental Table S1). Only TnT mutants had lower mitral early [E] and late [A] velocities, lower mitral annular velocity (E′) and pulmonary acceleration time (PAT/RR) suggestive of LV diastolic dysfunction (Fig. 1C and D, Supplemental Table S1), whereas both mutants had left atrial enlargement when compared to littermate controls (Supplemental Table S1).

To dissect genomic heterogeneity and explore the regulatory changes induced by these pathogenic variants in *Tnt2* and *Myh6*, we examined our previously published [13] RNA-seq data from 5-week-old mouse hearts. Compared to WT, a total of 9493 and 7408 genes were upregulated in TnT and MyHC mutants, respectively, with 4780 genes overlapping between the two mutants ($p < 0.05$, q < 0.01, FDR of 1 %). In contrast, 6288 and 8122 genes were down-regulated in TnT and MyHC mutants, respectively. For functional annotation and integrative analysis, we utilized both Reactome [67] and Gene Expression Omnibus (GEO) [68,69] databases to comprehensively assess differentially expressed protein-coding genes (DEGs) in R92W-TnT and R403Q-MyHC mutant hearts. We constructed enrichment plots for biological processes (Fig. 2A and B), and interactions between biological processes involved in DEGs were clustered according to their gene and pathway interactions (Fig. 2C and D). Functional enrichment analysis showed that many DEGs in TnT mutants were predominantly enriched in the Krebs cycle, respiratory electron transport, and branched-chain amino acid metabolism (Fig. 2A). In contrast, MyHC mutants primarily showed enrichment in

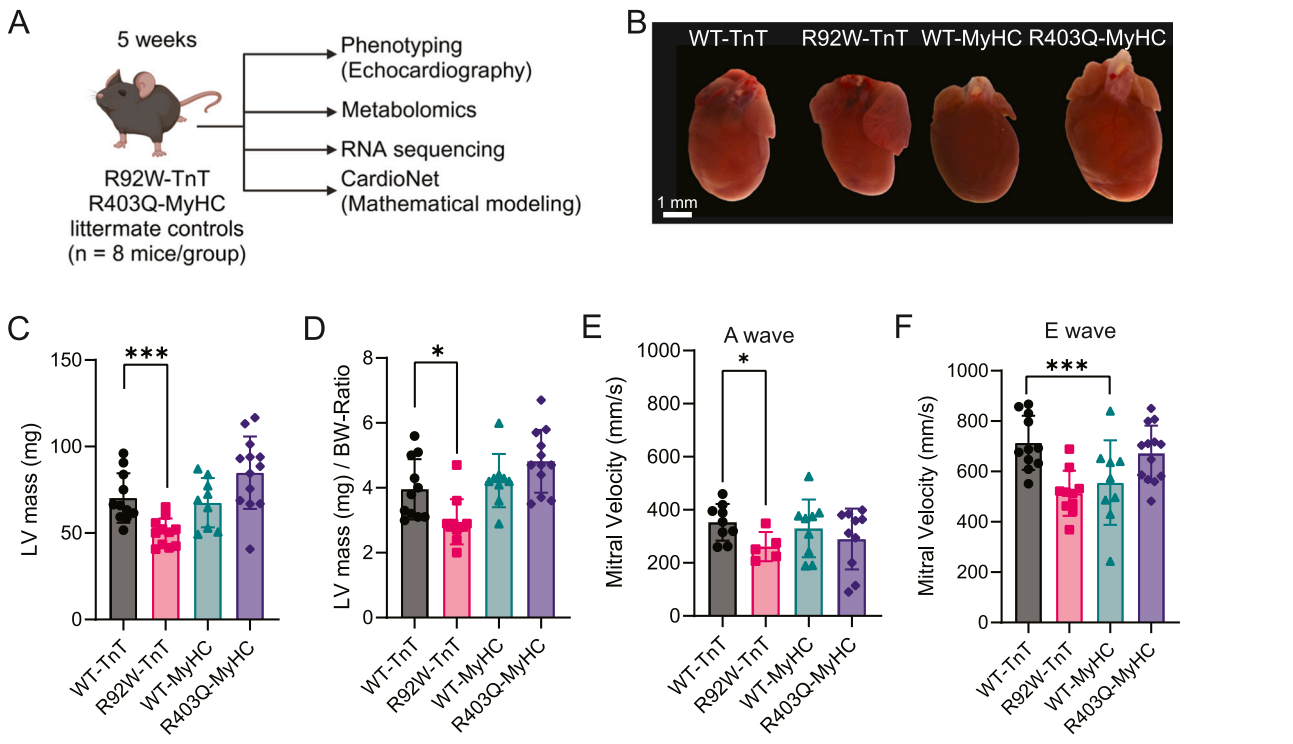

Fig. 1. Cardiac remodeling in 2 murine models of HCM at early disease stage. (A) Study design: Phenotyping and multi-omics in R92W-TnT and R403Q-MyHC mutant and littermate control hearts at 5 weeks of age. Hearts were collected for the extraction of primary metabolites, complex lipids, and biogenic amines. RNA-seq analysis, and untargeted metabolomics analysis using three different mass spectrometry (MS) platforms was followed by multi-omics network analysis and computer simulations, using CardioNet. (B) Representative gross anatomy from (R92W-TnT, R403Q-MyHC) mice and littermate controls (WT). Bi-atrial enlargement in R92W-TnT mutant heart is evident. (C–D) Echocardiographic assessment of R92W-TnT and R403Q-MyHC hearts. (C) Left ventricular (LV) mass was significantly lower in TnT mutants; (D) mitral A and E velocity were significantly lower only in TnT mutants. $n = 11$ mice/group. Wilcoxon rank sum test; *P*-value * < 0.05; *P*-value *** < 0.001. (Created with BioRender.com.)

liver-X-receptor (LXR) signaling, mitochondrial biogenesis, and calcium homeostasis (Fig. 2B). Taken together, these distinct transcription profiles suggest allele-specific metabolic changes.

3.2. *R92W-TnT and R403Q-MyHC differentially alter cardiac lipid composition*

To quantify metabolic alterations that could drive cardiac remodeling, we conducted an in-depth untargeted mass spectrometry (MS)-based metabolomics and lipidomics analysis (Fig. 3A) followed by pathway and network analysis to determine biological patterns [23–25,50]. Primary metabolites, biogenic amines, and lipids differ in their chemical properties; thus, we combined different chromatographic approaches to increase coverage of metabolite detection. We identified 891 metabolites in total (Fig. 3A), including 163 primary metabolites, 165 biogenic amines, and 558 complex lipids using a combination of gas chromatography (GC)-time of flight (TOF) MS, hydrophilic interaction chromatography (HILIC) TripleTOF MS/MS and charged surface hybrid (CSH) chromatography coupled to a quadrupole TOF MS/MS (CSH-QTOF MS/MS), respectively (Supplemental Tables 2–4). The variability between HCM models was analyzed by using principal component analysis (PCA). Among mutant-dependent separation, 64 % of the total variance was captured in the first two dimensions across R92W-TnT and R403Q-MyHC mice (Fig. 3B). The CSH-QTOF MS/MS analysis yielded a total of 514 unique lipid identifications for the MyHC and TnT cohorts across five lipid categories: phospholipids, sphingolipids, glycerolipids, fatty acids (FA), and sterols (Fig. 3C). Identified lipids comprised 237 phospholipids, 170 glycerolipids, 60 sphingolipids, 4 sterols, and 43 fatty acids across the TnT and MyHC cohort. The breakdown of lipid category designation into classes showed 5 phospholipids (phosphatidylinositols (PI), phosphatidylcholines (PC), phosphatidylethanolamines (PE), phosphatiylserine (PS), and cardiolipins (CL)), 3 sphingolipids (sphingomyelins (SM), ceramides (Cer) and N-acylsphingosines (Cer-NS)), 3 glycerolipids (triacylglycerolipids (TG), diacylglycerolipids (DG), and phosphatidylglycerol (PG)), 2 sterols (cholesterol and cholesteryl ester (CE)) and fatty acids (free fatty acids and acylcarnitines) (Fig. 3C).

We compared cardiac metabolites of R92W-TnT and R403Q-MyHC mice with WT, using Chemical Similarity Enrichment Analysis (ChemRICH) to identify differences in lipid and intermediary metabolite profiles [63]. Our analysis identified sets of metabolites based on their chemical ontologies and structural similarity (Fig. 4A and B), and results were visualized according to the overall chemical diversity and enrichment across all metabolites. We observed a stronger biological response in TnT-mutant hearts when compared to MyHC mutants: 40.4 % (271/670) of lipids and 24.7 % (81/328) of metabolites were significantly different ($p < 0.05$) in TnT mutants compared to WT, whereas 10.4 % (70/670) of lipids and 5.8 % (19/328) of metabolites were significantly different ($p < 0.05$) in MyHC mutants compared to WT. Both mutant hearts demonstrated significant alterations in levels of purine nucleosides, trisaccharidesand dicarboxylic acids, as well as lipid species including, acylcarnitines, phosphatidylethanolamines (PEs), phosphatidylinositols (PIs), ceramides (Cer), and triglycerides (TGs) (Fig. 4A and B). The R92W-TnT variant was associated with reduced abundance of nicotinamide (pyridines), adenine (purines), guanosine (purine nucleosides), leucine (branched-chain amino acids), alpha-ketoglutarate (Krebs cycle intermediate) indicating impaired energy provision, compared to littermate controls (Tables 1A and 1B, Supplemental Fig. S1A). In addition, R92W-TnT hearts demonstrated significantly altered 12 lipid metabolite sets with unsaturated PCs, unsaturated PEs, and unsaturated Cer on the one hand, and lower significance for saturated PCs, saturated lyso-PCs, and saturated Cer on the other hand (Tables 1A and 1B, Supplemental Fig. S1A). Additional diversity within

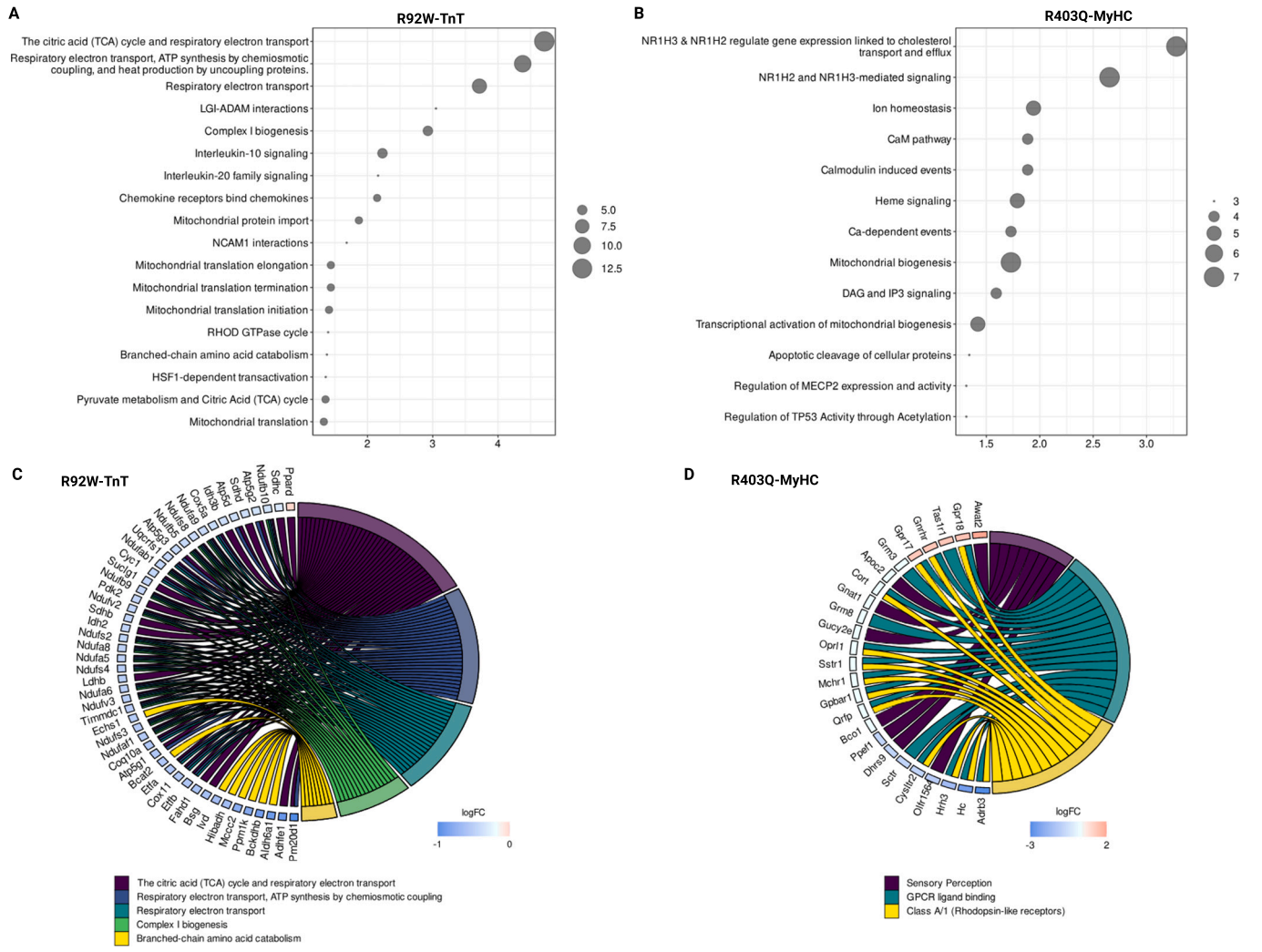

Fig. 2. Functional enrichment analysis of differentially expressed protein-coding genes in R92W-TnT and R403Q-MyHC mouse hearts, at early disease stage. (A–B) GEO database enrichment dot of significantly up- or down-regulated genes in response to (A) R92W-TnT or (B) R430Q-MyHC. Enrichment for GEO biological processes are depicted against *p*-value of expression. The dot size represents the number genes under a specific term ($n = 3$ mice/group). (C–D) GO cluster plot showing a chord dendrogram of the clustering of the expression spectrum of significantly up-or-downregulated genes in response to (C) R92W-TnT or (D) R430Q-MyHC variants.

phospholipids was observed in the fatty acid linkages, including alkenyl ether (plasmalogen, P-), alkyl ether (O-) and lysoacyl species (e.g., N-acyl-lyso and lyso species), as well as the glycosylation of sphingolipids. Of the identified lipids, marked difference was observed in statistical significance for acylcarnitine, ceramide (Cer) and cardiolipin (CL) levels (Supplemental Fig. S1A, Table 1A). Taken together, these results demonstrate cardiac metabolic and lipidomic remodeling in response to pathogenic variants in *Tnnt2* and *Myh6* genes. Furthermore, our data suggests that the R92W-TnT variant leads to significant impairment of oxidative metabolism that causes broad phospholipid alterations.

3.3. R92W-TnT and R403Q-MyHC impact the acyl-composition of phospholipids in HCM

In a next step, we investigated whether the acyl-chain composition and degree of saturation in acylcarnitine, ceramide and cardiolipin species contribute to the observed difference in metabolic profiles between TnT and MyHC mutant hearts. We quantified a shift in the incorporation of long-chain fatty acyl residues in acylcarnitine, ceramide and cardiolipin species (Fig. 5). Specifically, we identified lower abundance of unsaturated long-chain acyl-carnitines (18:1, 18:2 and 20:1) in both mutant mouse hearts, compared to WT (Fig. 5A and B). Next, we compared the fatty acyl chain composition and degree of saturation within the ceramide species (Fig. 5C and D). Cer d36:1 is the predominant ceramide species (>40 %) in hearts from WT mice followed by Cer d40:2 (25–30 %) (Fig. 5C). However, this relationship is shifted towards ceramide d40:2 in both mutants (35 % in TnT mutants, 45 % in MyHC mutants). The R403Q-MyHC variant is associated with a significantly higher contribution of Cer d40:2 compared to any other experimental group (Fig. 5D). The increase in fatty acyl chain length and degree of saturation is prominent in TnT mutants as indicated by increased contribution of Cer d40:0 and d42:0, which is unchanged in R403Q-MyHC mutants compared to littermate controls. The CL fraction was significantly impacted in R92W-TnT mice with a dominant shift from CL 76:12 towards CL 72:7 (Fig. 5E and F). In control mice, CL76:12 and CL72:7 represent on average 18 % and 8 % of the total CL fraction. This relationship contrasts with TnT mutants, with CL76:12 and CL72:7 representing on average 10 % and 15 %, respectively, whereas the CL composition was similar in MyHC mutants and WT. Taken together, we observed selective enrichment of FA18:0 in Cer and CL species in TnT mutant hearts, which could underlie differences in cardiac metabolites and mitochondrial function observed between TnT and MyHC mutant hearts at early disease stage.

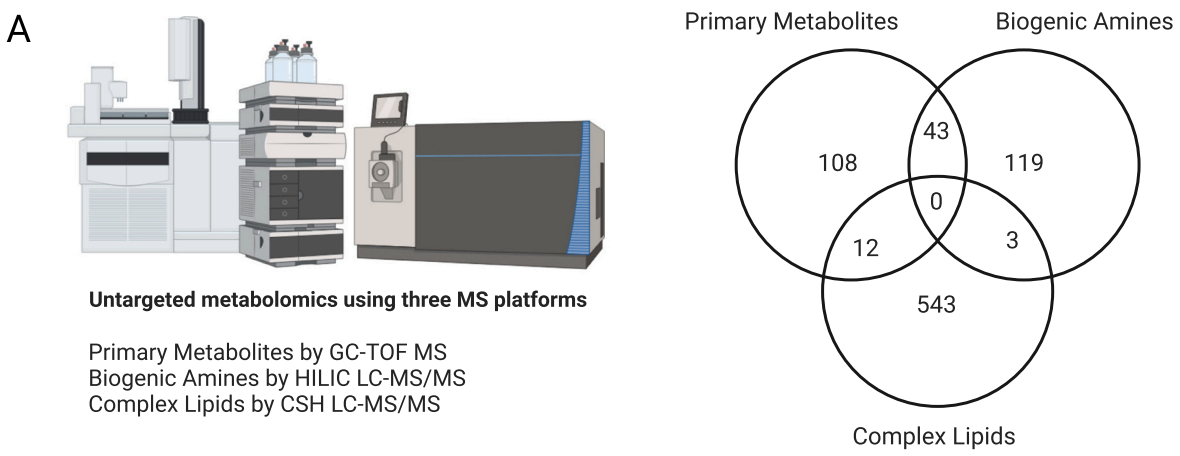

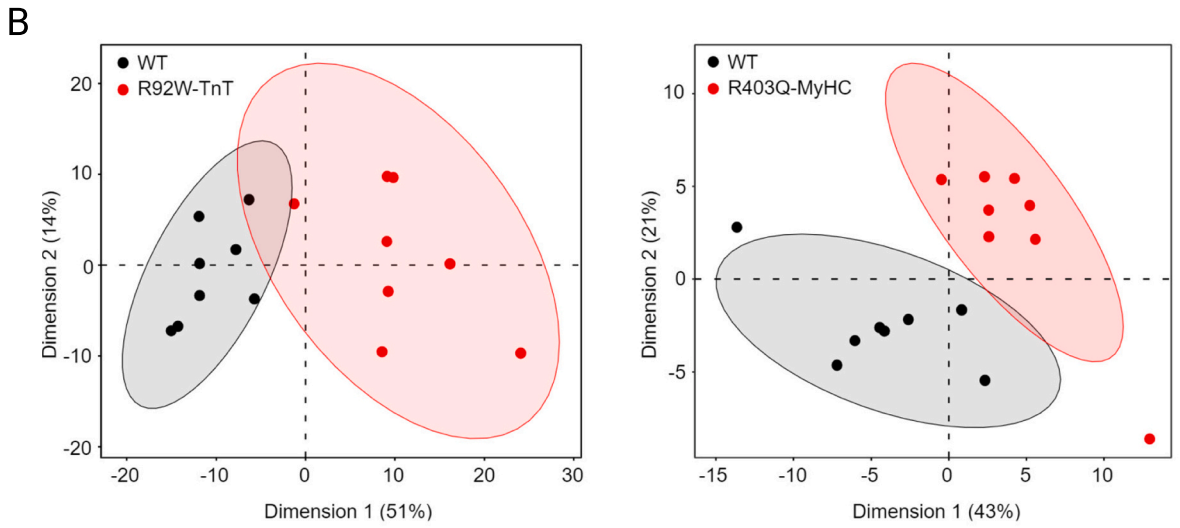

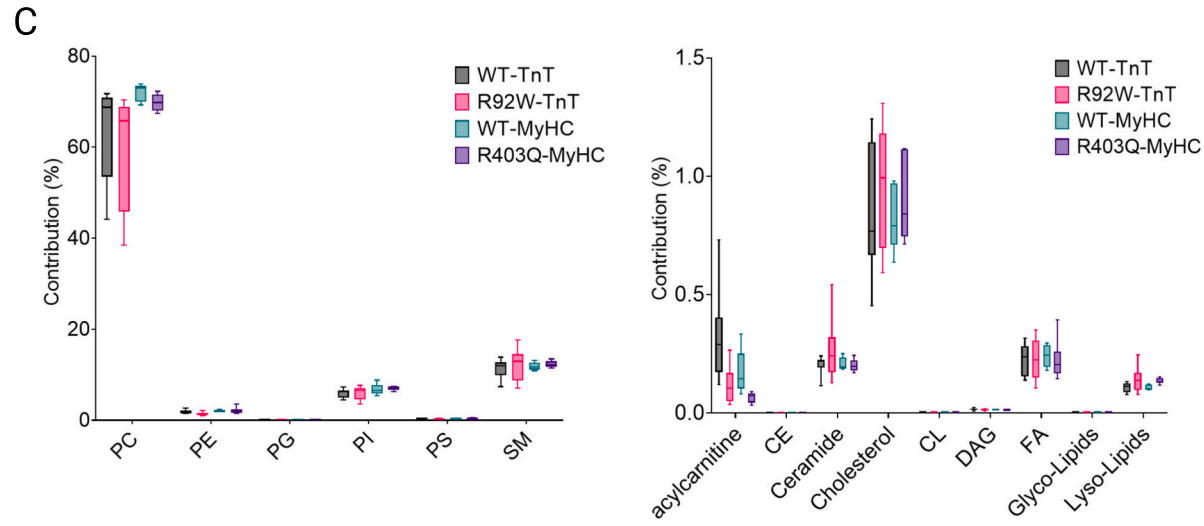

Fig. 3. Metabolic and lipidomic profiling R92W-TnT and R403Q-MyHC mutant mouse hears, at early disease stage. (A) Three different mass spectrometry (MS) platforms were used for untargeted metabolomics and lipidomics of heart tissue in R92W-TnT and R403Q-MyHC mouse models. A total of 891 metabolites; with 163 total metabolites found in gas chromatography (GC)-time of flight (TOF) MS, 165 metabolites found in liquid chromatography (LC)-MS/MS analysis, and 563 metabolites found in charged surface hybrid (CSH) LC-MS/MS lipidomics. (B) Principal component analysis of the metabolome and lipidome from heart tissue in R92W-TnT and R403Q-MyHC mice. Dimensions 1 and 2 explain 64 % of the variance in both genotypes. $n = 8$ mice/group. (C) Phospholipid (left panel) and overall lipid composition (right panel) in MyHC and TnT mutants. The contribution of phospholipid species is depicted in relation to the total phospholipid fraction. No difference was observed in each phospholipid or lipid species in the two mutants when compared to respective WT. 2-way ANOVA with Tukey's multiple comparison test. n = 8 mice/group. Abbreviations: SM, sphingomyelin; PC, phosphatidylcholine; PE, Phosphatidylethanolamine; PG, phosphatidylglycerol; PI, phosphatidylinositol.

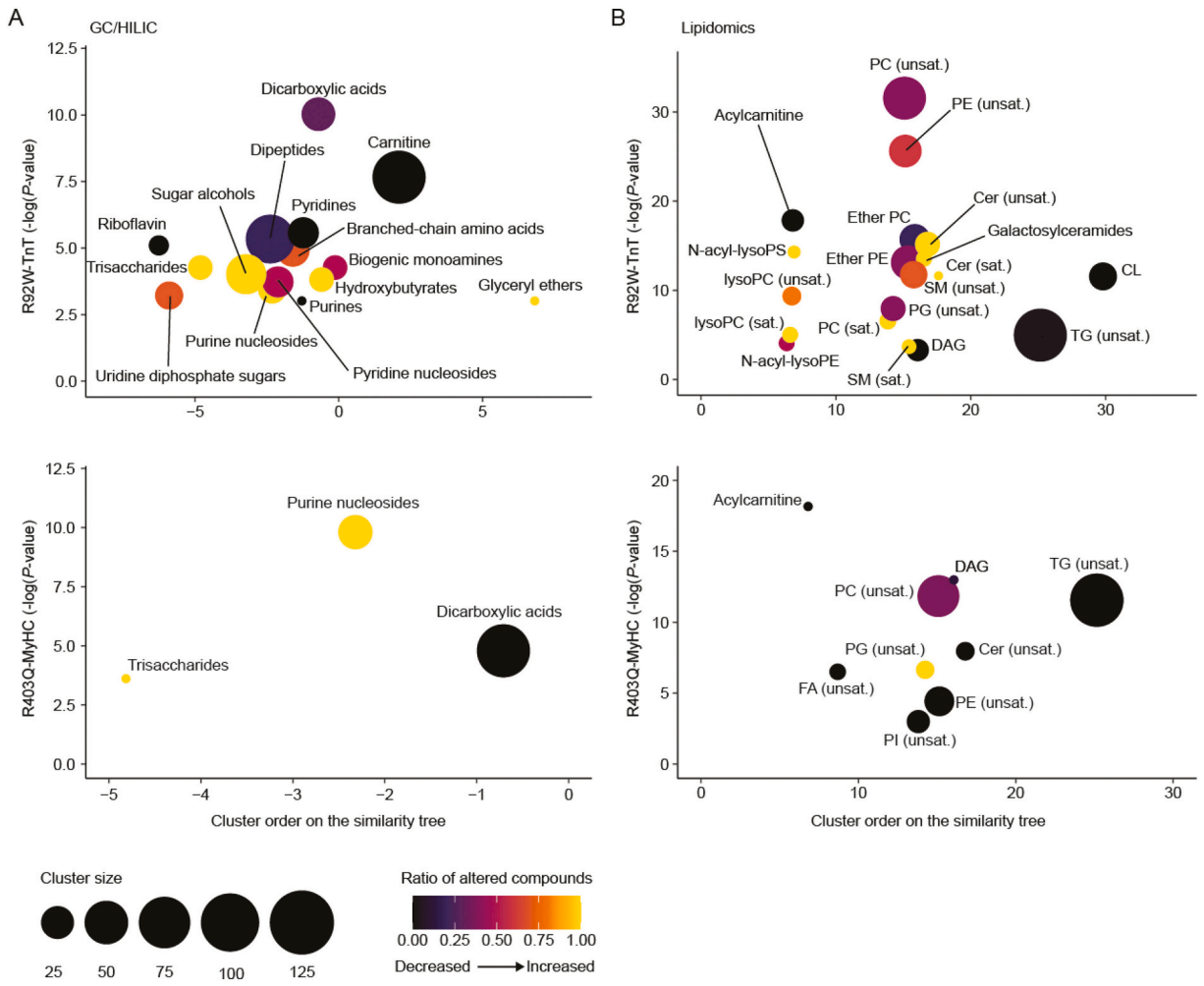

Fig. 4. Pathogenic variants in sarcomeric protein genes promote cardiac metabolic remodeling at early disease stage. (A–B) ChemRICH set enrichment plots for GC–MS and LC-MS/MS-based metabolomics (B) and CSH LC-MS/MS lipidomics (B). Each node depicts a significantly altered metabolite cluster. Node sizes and colors represent the total number of metabolites and proportion of increased or decreased compounds in each cluster, respectively. Cer, ceramides; CL, cardiolipins; PC, phosphatidylcholines; PE, phosphatidylethanolamines; PS, phosphatidylserines; SM, sphingomyelins; TG, triglycerides; sat., saturated; unsat., unsaturated.

3.4. Mathematical flux analysis identifies differential metabolic dependencies in R92W-TnT and R403Q-MyHC

Changes in metabolite and lipid abundances can either result from differential production or utilization of a given intermediate due to higher flux from synthesizing reactions or decreased flux towards consuming reactions. To assess the impact of pathogenic variants in TnT and MyHC on cardiac metabolism, we conducted mathematical modeling using CardioNet [30]. This computational approach allows the prediction and identification of metabolic fluxes by integrating experimental data, including from metabolomics and lipidomics analyses [70,71]. We determined flux distributions using flux balance analysis (FBA), which applies a steady-state assumption while optimizing an objective function (see Methods for details). The linear optimization problem was to maximize ATP provision and ensure biomass synthesis (e.g., protein, lipid synthesis) while fulfilling a set of constraints defined by the metabolic profile in mutant and WT hearts. Annotation enrichment of observed clusters and unsupervised hierarchical cluster analysis (Supplemental Fig. S2A and B) demonstrated distinct metabolic remodeling in R92W-TnT and R403Q-MyHC hearts, consistent with our multi-omics analysis. Simulations of TnT mutants revealed upregulation of lipid metabolism as reflected in cluster 2 and cluster 3 (Supplemental Fig. S2A and B).

To understand the predicted metabolic flux distributions, we first annotated identified reactions to curated pathways within the CardioNet database. Unsupervised hierarchical clustering of calculated flux rates separated TnT and MyHC mutants from WT mice (Fig. 6A). We identified an increased flux contribution in fructose, ribose, and glucose metabolism in TnT mutants, which combine glycolysis, oxidative and non-oxidative pentose phosphate pathway, and nucleotide synthesis. Furthermore, we found increased flux distributions in fatty acid biosynthesis and lipid metabolism consistent with our lipidomics data (Fig. 6A). Overall oxidative phosphorylation was lower in TnT and MyHC mutants compared to WT (Fig. 6A). To understand the metabolic fate of energy-providing substrates, we analyzed the contribution of glucose and fatty acid utilization. Glucose uptake and utilization is predicted to increase (1.5-fold) in TnT mutants and decrease (0.7-fold) in MyHC mutants when compared to WT (Fig. 6B). Our simulations also predicted higher uptake of linoleate (FA18:2) and linolenate (18:3) in both mutants, when compared to WT (Fig. 6B). In TnT mutants, FA18:2 oxidation is increased while FA22:5 and FA22:6 oxidation is decreased compared to control, and MyHC mutants (Fig. 6C). The per carbon ATP yield from FA22:5 and FA22:6 is significantly higher compared to FA18:2 and glucose indicating that MyHC mutant and WT mice rely more on ATP provision from fatty acids compared to TnT mutants. These findings are further supported by network analysis and visualization (Fig. 6D). Increased lipid remodeling and synthesis in TnT mutants requires compensatory flux changes to ensure adequate provision of

Table 1A
R92W-TnT vs Littermate Control (WT) Mice.

Morphometric data			
Parameter	Control TnT (n = 8) Mean ± SD	R92W-TnT (n = 8) Mean ± SD	p value
Mouse weight (g)	20.25 ± 1.58	19.33 ± 2.36	0.38
Heart weight (mg)	131.09 ± 29.93	129.48 ± 27	0.91
HW/MW ratio	0.0064 ± 0.001	0.0067 ± 0.001	0.62

Differentially expressed lipids and metabolites	FDR p value	Log_2 FC
Lipids		
GlcCer (d14:14E_20:02OH)	0.04	3.8
LPC (p-18:0) or LPC (o-18:1)	0.04	2.4
PC (37:1)	0.04	1.97
Cer-NS (d42:1) or Cer-NS (d18:1_24:0)	0.04	1.51
Ceramide (d34:2)	0.04	1.27
PC (32:3)	0.04	1.16
PC (30:0)	0.04	1
SM (d36:3)	0.04	0.9
PE (p-36:4) or PE (o-36:5)	0.04	0.85
Cer (d42:2) B	0.04	0.83
GlcCer (d41:1)	0.04	0.82
LNAPS (38:4)	0.04	0.62
LNAPS (42:9)	0.04	0.55
PE (38:4) C	0.04	0.55
PG (35:1) or PG (16:0_19:1)	0.04	0.51
SM (d34:1)	0.04	0.49
PC (40:6) B	0.04	−0.36
PC (38:6) B	0.04	−0.39
TAG (56:7) A	0.04	−0.45
PC (37:6)	0.04	−0.48
PC (39:7)	0.04	−0.48
PE (40:9) or PE (18:3_22:6)	0.04	−0.5
PG (40:5) or PG (18:0_22:5)	0.04	−0.51
PC (38:7)	0.04	−0.52
PE (42:8e) or PE (20:2e_22:6)	0.04	−0.52
PC (40:7)	0.04	−0.54
PC (40:7e) or PC (18:1e_22:6)	0.04	−0.55
TAG (40:0)	0.04	−0.56
SM (d38:1)	0.04	−0.57
HBMP (18:1_18:2_16:0)	0.04	−0.59
PC (40:5) B	0.04	−0.59
PC (p-38:6) or PC (o-38:7)	0.04	−0.62
PC (p-38:5) or PC (o-38:6) A	0.04	−0.63
TAG (58:7) or TAG (18:1_18:2_22:4)	0.04	−0.63
PE (38:7e) or PE (18:3e_20:4)	0.04	−0.64
PG (32:0)	0.04	−0.64
PC (40:8e) or PC (18:2e_22:6)	0.04	−0.65
TAG (58:8)	0.04	−0.65
PC (40:9)	0.04	−0.71
PE (42:7e) or PE (20:1e_22:6)	0.04	−0.74
TAG (58:8) or TAG (18:1_18:2_22:5)	0.04	−0.74
PC (44:12) or PC (22:6_22:6)	0.04	−0.78
PC (40:8)	0.04	−0.82
TAG (58:10) A	0.04	−0.82
PE (40:8) or PE (18:2_22:6)	0.04	−0.83
PE (40:8)	0.04	−0.84
PC (p-38:5) or PC (o-38:6) A	0.04	−0.86
TAG (58:11)	0.04	−0.89
TAG (58:9) or TAG (18:2_18:2_22:5)	0.04	−0.89
TAG (58:9)	0.04	−0.94
PC (40:8)	0.04	−0.97
PC (38:7e) or PC (16:1e_22:6)	0.04	−0.98
TAG (62:14)	0.04	−1
CL (72:9) or CL (18:2_18:2_18:2_18:3)	0.04	−1.03
Acylcarnitine (22:1)	0.04	−1.11
TAG (58:10) or TAG (18:2_18:2_22:6)	0.04	−1.14
PG (40:6) or PG (18:0_22:6)	0.04	−1.2
PC (42:11)	0.04	−1.24
CL (78:15) or CL (18:2_20:5_18:2_22:6)	0.04	−1.32
Acylcarnitine (20:1)	0.04	−1.58
Acylcarnitine (18:1)	0.04	−1.75
Acylcarnitine (18:2)	0.04	−1.82
CL (76:12) or CL (18:2_18:2_18:2_22:6)	0.04	−2.08
PE (34:1e) or PE (16:0e_18:1)	0.04	−4.38

Table 1A (*continued*)

Differentially expressed lipids and metabolites	FDR p value	Log_2 FC
Metabolites		
Isohexonic acid	0.02	1.62
N-acetyl-D-hexosamine	0.02	1.53
Proline	0.03	1.33
Guanosine	0.02	1.18
Galacturonic acid	0.04	0.96
Serine	0.04	0.95
Alpha-aminoadipic acid	0.04	0.92
Myo-inositol	0.02	0.89
Isoleucine	0.02	0.79
Leucine	0.03	0.67
Oxalic acid	0.03	0.67
Cellobiose	0.04	0.67
Indole-3-lactate	0.04	0.64
Xylitol	0.04	0.61
Inosine	0.03	0.55
Fumaric acid	0.02	−0.66
Pantothenic acid	0.03	−1.02
Succinic acid	0.03	−1.26
Lactobionic acid	0.02	−1.33
Alpha-ketoglutarate	0.03	−1.74

Table 1B
R403Q-MyHC vs littermate control (WT) mice.

Morphometric data			
Parameter	Control MyHC (n = 8) Mean ± SD	R403Q-MyHC (n = 8) Mean ± SD	p value
Mouse weight (g)	20.35 ± 2.23	20.30 ± 1.83	0.97
Heart weight (mg)	122.8 ± 14.06	150.92 ± 44.67	0.12
HW/MW ratio	0.006 ± 0.0003	0.0073 ± 0.0016	0.06

Differentially expressed lipids and metabolites	Non-adjusted p-value	Log_2 FC
Lipids		
DAG (38:6) A	0.005	−0.31
SM (d40:2) A	0.010	−0.43
PC (35:3)	0.010	−0.52
DAG (40:8) or DAG (18:2_22:6)	0.004	−0.57
PI (34:2) or PI (16:0_18:2)	0.007	−0.61
TAG (58:10) A	0.010	−0.67
DAG (36:4) A	0.005	−0.71
Acylcarnitine (10:0)	0.005	−0.99
Acylcarnitine (14:2)	0.007	−1.05
Acylcarnitine (20:1)	0.010	−1.44
Acylcarnitine (18:2)	0.010	−1.7
Acylcarnitine (18:1)	0.007	−1.79
Linoleic acid	0.010	−0.65
Oleic acid	0.005	−0.83
3-Hydroxypalmitic acid	0.004	−1.21
Metabolites		
Maltotriose	0.001	1.04
Guanosine	0.007	0.88
Anserine	0.010	−1.66

There were no lipids or metabolites with adjusted (FDR) $p < 0.05$ in the R943Q-MyHC vs WT comparison, so we only present compounds with non-adjusted $p < 0.05$ for R943Q-MyHC vs WT comparison.
Abbreviations: GlcCer is glucosylceramide, LPC is lysophosphatidylcholine, PC is phosphatidylcholine, Cer-NS is ceramide non-hydroxyfatty acid-sphingosine, SM is sphingomyelin, PE is phosphatidylethanolamine, Cer is ceramide, LNAPS is N-acyl-lysophosphatidylserine, PG is phosphatidylglycerol, TAG is tri-acylglycerol, HBMP is hemibismonoacylglycerophosphate, CL is cardiolipin, DAG is diacylglycerol, and PI is phosphatidylinositol.

reducing equivalents in the form of NADH and NADPH. Taken together, our simulations suggest that energy provision and substrate utilization is differentially impacted in R92W-TnT and R403Q-MyHC mutants. TnT mutants are negatively impacted by a mismatch between oxidative and

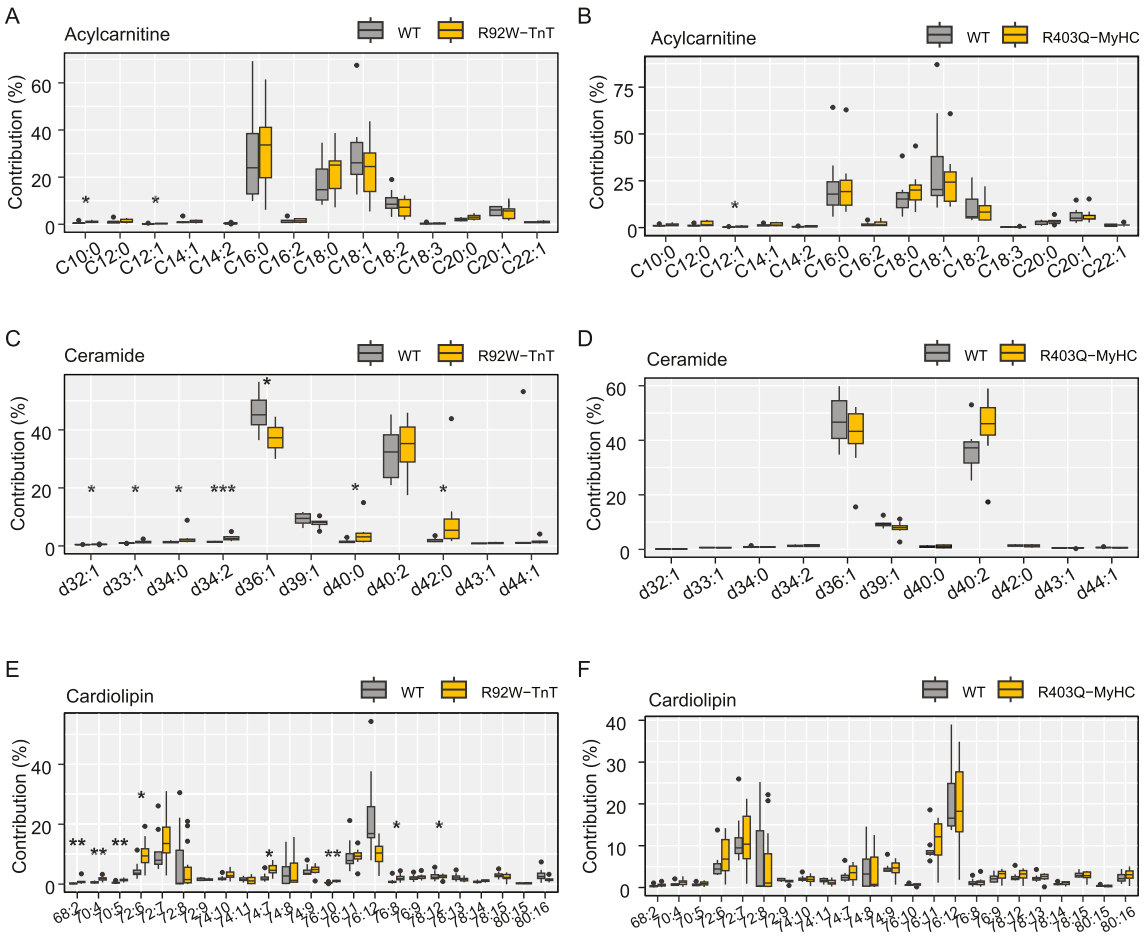

Fig. 5. Fatty acyl-chain composition and degree of unsaturation in ceramide, acylcarnitine and cardiolipin species in HCM mouse hearts at early disease stage. (A–B) Acylcarnitine composition in R92W-TnT (A) and R403Q-MyHC (B) hearts compared to littermate controls. (C–D) Ceramide composition in R92W-TnT (C) and R403Q-MyHC (D) hearts compared to littermate controls. (E–F) Cardiolipin composition in R92W-TnT (E) and R403Q-MyHC (F) hearts compared to littermate controls. n = 8 mice/group. P-value: * < 0.05; ** < 0.01.

reductive demands as evidenced by a metabolic nutrient shift from increased fatty acid towards glucose utilization.

3.5. Allele-specific differences in oxidative stress at early disease stage

Computational modeling revealed increased flux in lipid metabolism. Specifically, CardioNet simulations predicted an increased peroxidation of PS and PE in the lysosome and microsome (combined compartment of endoplasmic reticulum and golgi apparatus) (Fig. 7A). Increased lipid peroxidation is potentially associated with an increased oxidative stress. To test this hypothesis, we quantified oxidative-induced lipid peroxidation using 4-hydroxynonenal (4-HNE) as a marker protein (Fig. 7B). 4-HNE is an electrophilic molecule that can easily diffuse across membranes, is highly reactive towards nucleophilic thiol and amino groups, and is a major generator of oxidative stress. TnT mutant hearts had higher abundance of 4-HNE compared to littermate controls, whereas no difference in 4-HNE was observed between MyHC mutants and littermate controls (Fig. 7B).

4. Discussion

Our systems biology approach revealed distinct metabolic landscapes in R92W-TnT and R403Q-MyHC hearts at early disease stage, that could provide a mechanistic framework for phenotypic variability in HCM. At early disease stage, R92W-TnT hearts have bi-atrial enlargement, LV diastolic dysfunction, significant impairment of energy substrate metabolism, phospholipid remodeling and evidence of lipid peroxidation, whereas R403Q-MyHC hearts have a mild phenotype reflected by preserved energy substrate and phospholipid metabolism (Tables 1A and 1B, Figs. 1 and 4). Our computer simulations predict decreased oxidative phosphorylation and upregulation of glycolysis in TnT mutants, which could lead to reduced contractile reserve, energetic stress and diastolic dysfunction, which are commonly seen in human HCM [72–74]. Interestingly, mutant MyHC hearts showed a trend towards higher LV mass and small changes in the cardiac metabolome and lipidome, suggesting that myocyte hypertrophy and metabolic remodeling occur in parallel in early disease stage of HCM.

We combined RNA-sequencing and metabolomics with computational modeling using CardioNet [53,59,70,71,75] to identify flux distributions that could explain the observed metabolic patterns. CardioNet predicts an increased contribution of glycolysis and the pentose phosphate pathway towards ATP provision and reductive metabolism, along with reduction in oxidative phosphorylation in R92W-TnT hearts (Fig. 6D). In contrast, mathematical simulations of R403Q-MyHC metabolism indicate that the observed metabolic changes are compensatory flux changes likely protecting R403Q-MyHC hearts (Fig. 6D). Thus, our systems biology approach using CardioNet reveals allele-specific flux changes and provides a mechanistic understanding of metabolomics studies.

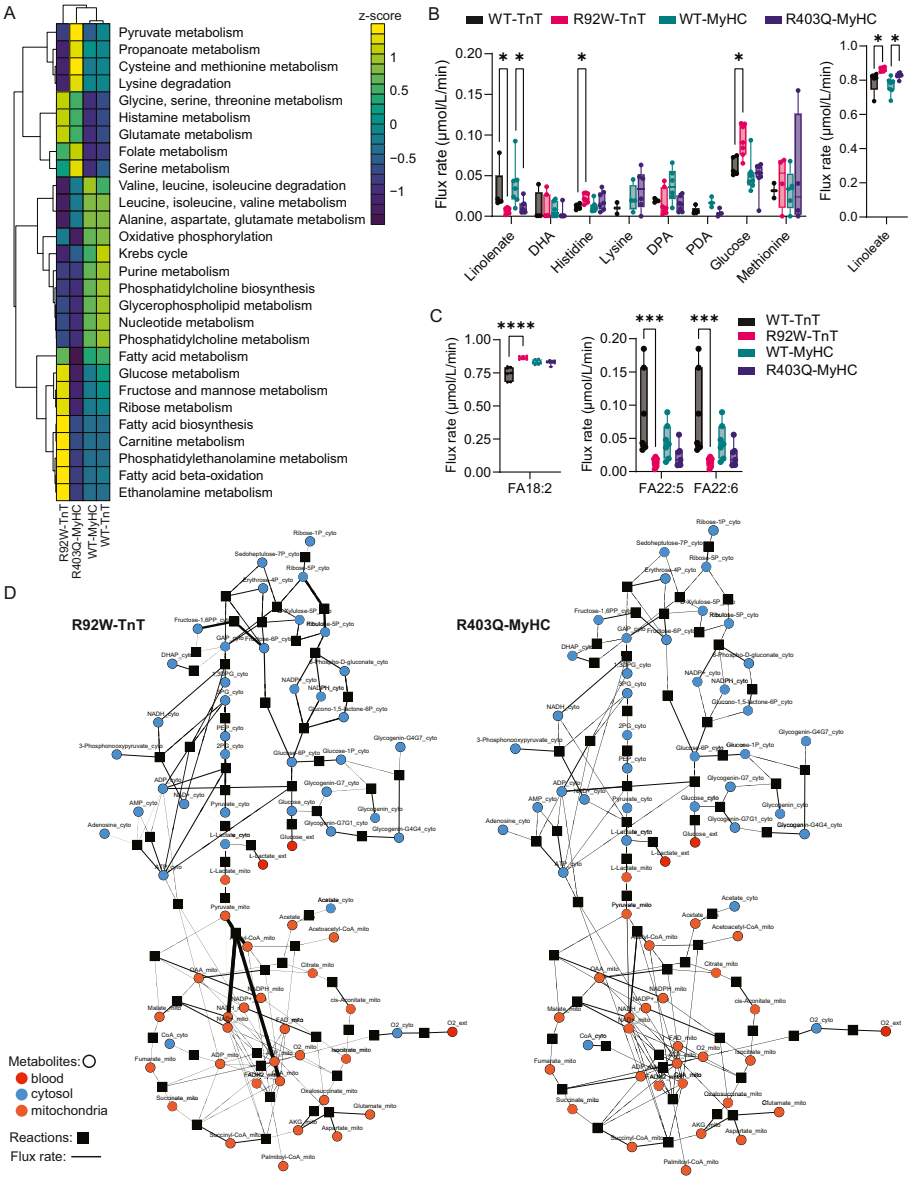

Fig. 6. Analysis of flux alterations in R92W-TnT and R403Q-MyHC using CardioNet at early disease stage. (A) Metabolic flux distributions were calculated using CardioNet and constrained-base modeling using optimization algorithms. Reactions were assigned to pathways and predicted fluxes were summed across pathways for unsupervised hierarchical cluster analysis. (B) Predicted uptake rates of extracellular metabolites across experimental groups. Flux rates were calculated using CardioNet simulations for R92W-TnT, R403Q-MyHC and WT mouse hearts. (C) Flux rate predictions for fatty acid β-oxidation for linoleate (FA18:2), docosapentaenoic acid (DPA; FA22:5), and docosahexaenoic acid (DHA, FA22:6) in both mutants compared to WT. (D) Visualization of predicted flux rates for glycolysis, pentose phosphate pathway and Krebs cycle. Edge thickness is scaled to calculated flux rates. $n = 8$ mice/group. ANOVA with multiple comparison analysis. FDR < 1 %.

4.1. Abnormal cardiolipin composition in R92W-TnT$^{+/-}$ hearts

In humans, the R92W-TnT variant is associated with mild or no cardiac hypertrophy [33] and sudden cardiac death at a young age [76], whereas the R403Q-MyHC variant is associated with moderate cardiac hypertrophy and heart failure requiring transplantation in middle age [34]. At early disease stage, R92W-TnT and R403Q-MyHC mouse hearts are characterized by distinct cardiac phenotypes and metabolic alterations impacting phospholipid metabolism, which contrast the well-accepted notion of enhanced glycolysis in the setting of hypertrophic remodeling (Fig. 5). We observed a notable shift in the total abundance and acyl-chain composition of cardiolipin (CL) in mutant TnT hearts. Incorporation of FA18:0 and FA18:1 in CL was increased when compared to FA18:2 in TnT mutants. Cardiolipin is the most critical phospholipid of the inner mitochondrial membrane and is directly involved in mitochondrial function [77]. In addition to PE, CL interacts with and stabilizes electron transport chain (ETC) complexes and supports mitochondrial cristae formation [78]. Studies in human and murine tissue demonstrate that CL acyl-chain composition is highly tissue-specific [78–80]. Heart tissue is characterized by preferential incorporation of linoleic acid (FA18:2) [81]. Our R92W-TnT mutant model exhibits increased abundance of FA18:0 and FA18:1 in CL, suggesting that the incorporation of FA18:2 is impaired. Alterations in the abundance and acyl-chain composition of CL in mitochondrial membranes can have functional consequences on electron transport chain function and ATP synthesis. The changes in mitochondrial phospholipid composition detected by our study in TnT mutant hearts could explain the molecular cardiac phenotype that we previously described [13] at early disease stage, characterized by lower mitochondrial complex I RCR, abnormalities in mitochondrial Ca^{2+}handling and reduced

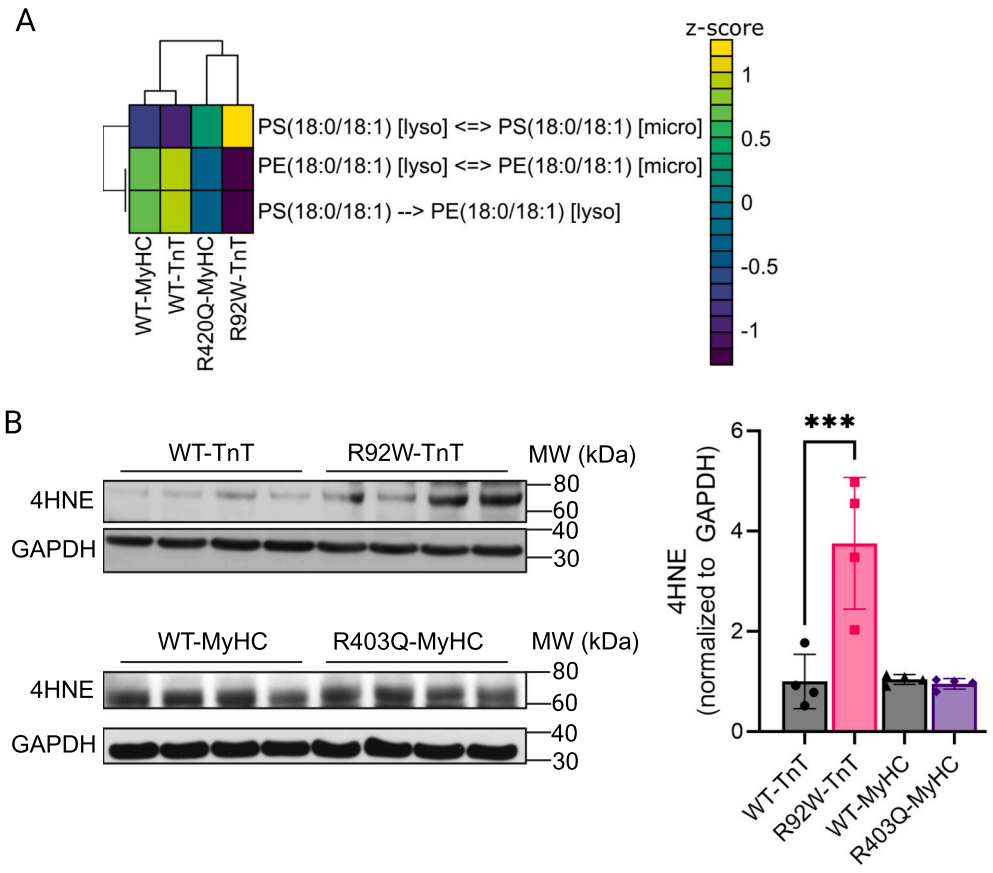

Fig. 7. Phospholipid metabolism drives oxidative stress in R92W-TnT hearts. (A) Summary of predicted flux rates for modifications of peroxidation of PS and PE in the lysosome (lyso) and microsome (micro; endoplasmic reticulum and golgi apparatus). (B) Quantification of lipid peroxidation using 4-hydroxynonenal (4-HNE) and western blotting. Densitometry was normalized to total GAPDH abundance. $n = 4$ mice/group. 2-way ANOVA and Tukey's posthoc multiple comparisons analysis. FDR < 1 %; ***q-value<0.005.

mitochondrial DNA copy number [13]. Mitochondrial dysfunction predisposes to the development of energy deficits at high workloads, such as during exercise, which can lead to sustained ventricular arrhythmias and sudden cardiac death [17,82,83].

4.2. *Abnormal cytoplasmic Ca^{2+} dynamics could link mutant sarcomeric protein expression with changes in cardiac energy metabolism in R92W-TnT$^{+/-}$ mutants*

Calcium coordinately regulates ATP-consuming myofilaments and ATP-generating oxidative phosphorylation in the heart [17]. Calcium is released from the sarcoplasmic reticulum (SR) into the cytoplasm, where it binds troponin C to initiate contraction and is taken up by mitochondria, where it stimulates Krebs cycle dehydrogenases and complex V (*F0F1*-ATPase) of the ETC. Increased myofilament Ca^{2+}sensitivity resulting from the R92W-TnT variants is predicted [84] to increase myofilament Ca^{2+}binding, resulting in greater cytosolic Ca^{2+}buffering, lower peak systolic Ca^{2+}, higher peak tension, slower myofilament Ca^{2+}dissociation, higher diastolic calcium [84], positive inotropy and negative lusitropy – these computer modeling results are confirmed by Ca^{2+} measurements in isolated R92W-TnT$^{+/-}$ myocytes [40] and our echocardiography data in TnT mutants (Suppl Table S1). Higher cytoplasmic Ca^{2+} buffering in TnT mutant myocytes would be expected to reduce mitochondrial Ca^{2+} uptake and NADH generation, which fuels the ETC, resulting in reduced energy provision (predicted by CardioNet in this study - Fig. 6A). NADH is also important in mitochondrial antioxidant defenses, because of its conversion to NADPH. Hence, reduced mitochondrial NADH generation could contribute to mitochondrial oxidative stress and dysfunction, further depressing energy metabolism in TnT mutants. In the case of R403Q-MyHC$^{+/-}$, Ca^{2+} is thought to play a role in the induction of the hypertrophic response [44,85]. Dysregulation of SR Ca^{2+} handling, with reduced SR-Ca^{2+} stores is evident at four weeks [85], but is not associated with changes in diastolic Ca^{2+} and Ca^{2+} transients at early disease stage [44]. Together, these findings could explain the milder metabolic phenotype observed in our study. Fatkin et al. [44], hypothesize that the R403Q-MyHC$^{+/-}$ contractile apparatus functions as an "ion trap", leading to Ca^{2+} retention in the sarcomere, which would lead to reduced mitochondrial Ca^{2+} uptake, Krebs cycle, and oxidative phosphorylation flux (which is predicted by CardioNet -Fig. 6A).

4.3. *Comparison of mouse and human metabolomics study results*

Clinically, HCM patients are classified into three hemodynamic groups, namely, obstructive, non-obstructive and labile obstructive, based on the presence/absence of LV obstruction at rest and with provocation [72]. Patients can have non-obstructive hemodynamics at the early disease stage that can either progress to obstructive HCM or continue as non-obstructive HCM at the established disease stage. Surgical septal myectomy [14,86] and alcohol septal ablation were the only treatment options for patients with symptomatic LV obstruction that was unrelieved by medical therapy until the recent introduction of the cardiac myosin inhibitor Mavacamten [87]. Multi-omics profiling of myectomy tissue from HCM patients has revealed dysregulation of fatty acid oxidation, Krebs cycle, oxidative phosphorylation, and energy compromise [27,28], like R92W-TnT hearts at early disease stage. Human HCM hearts showed a significant decrease in the abundance of acylcarnitines [27,28], which is also evident in R92W-TnT and R403Q-

MyHC mouse hearts. Additionally, human HCM myocardium demonstrated increases in PCs, PEs, lyso-PCs, lyso-PEs, ceramides, reduction in TAG, and increased lipid peroxidation [28], like our results in R92W-TnT mouse hearts. The most notable difference between our results in HCM mouse models and HCM patient studies is the presence of genotype-specific metabolic remodeling in mouse hearts and the absence of correlation between genotype and cardiac metabolomic profile in human myectomy tissue [27–29]. There are several possible reasons for the differences in results between mouse and human metabolomics studies, including 1) disease stage: early disease stage in HCM mouse models and established disease stage in HCM patients; 2) cardiac physiology: non-obstructive HCM in mouse models, and obstructive HCM in patients undergoing septal reduction surgery (myectomy) [88]. These results lead us to hypothesize that LV obstruction induces convergence to a common cardiac metabolic phenotype in HCM. Non-invasive investigation of cardiac metabolism [89] that combines cardiac metabolic flux imaging with plasma profiling [90] in early-stage human HCM could be helpful to confirm our results of genotype-specific metabolic remodeling and to examine the association between metabolic, structural, and functional remodeling in human HCM.

4.4. Limitations

Our studies characterizing cardiac metabolomics at the early disease stage were undertaken only in mouse models because obtaining biopsies from asymptomatic patients with early-stage HCM is unethical. Our studies in mouse models cannot be directly translated to humans because of differences in mouse and human cardiac physiology, as well as differences in the dominant myosin heavy chain phenotype (α-MyHC in mice and β-MyHC in human) ventricular myocardium. The large number of unidentified metabolites inherently limits untargeted metabolomics. These compounds are frequently products of biotransformation and unspecific enzymatic reactions that physiologically occur but lead to 'unknowns' in LC-MS or GC–MS profiling scans. These compounds are not integrated into curated databases (e.g., HMDB, PubChem, KEGG), and often verified standards are missing. Furthermore, lipids are underrepresented in pathway-based databases, which limits pathway enrichment analysis. Therefore, we expanded our analysis using CardioNet, which includes cardiac-specific metabolic and lipidomic pathways. Another limitation of this study is the exclusion of unknown metabolites in our analysis. >80 % of metabolites are unknown in untargeted metabolomics workflows, and structural resolution is limited. Therefore, we are reporting our entire dataset in the supplementary materials to engage with the scientific community and address this chemical complexity. Lastly, due to a lack of method development, targeted assays for nicotinamide adenine dinucleotide (NAD), such as NAD+/NADH, could not be utilized in this study. Our metabolomics analysis yields high confidence data including MS and MS/MS data which provides a resource for the field. Lastly, this study does not clarify the transcriptional regulation of metabolic remodeling in early stage non-obstructive HCM. Multi-omic RNA-seq/ATAC-seq studies [91] could be helpful to address this question.

5. Conclusions

Multi-omics investigation, including comprehensive untargeted cardiac metabolomics and mathematical modeling revealed allele-specific differences in cardiac metabolism, with R92W-TnT$^{+/-}$ mutants demonstrating greater metabolic and lipidomic remodeling than MyHC mutants, as well as reduction in energy provision at early disease stage. Only TnT mutants showed enrichment of FA18:0 in cardiolipin species, which could lead to mitochondrial dysfunction, energetic stress and diastolic dysfunction. Our results in mouse models demonstrate the need for in vivo imaging of cardiac metabolic flux in early-stage human HCM to enable individualized interventions that mitigate oxidative stress, deleterious phospholipid remodeling and restore energy metabolism in HCM hearts.

CRediT authorship contribution statement

Arpana Vaniya: Writing – review & editing, Writing – original draft, Visualization, Validation, Software, Methodology, Investigation, Formal analysis, Data curation. **Anja Karlstaedt:** Writing – review & editing, Writing – original draft, Visualization, Validation, Supervision, Software, Resources, Project administration, Methodology, Investigation, Formal analysis, Data curation, Conceptualization. **Damla Gulkok:** Visualization, Validation, Software, Investigation, Formal analysis, Data curation. **Tilo Thottakara:** Writing – review & editing, Writing – original draft, Validation, Software, Methodology, Investigation, Formal analysis. **Yamin Liu:** Formal analysis, Visualization. **Sili Fan:** Formal analysis. **Hannah Eades:** Formal analysis. **Styliani Vakrou:** Formal analysis. **Ryuya Fukunaga:** Writing – original draft, Writing – review & editing. **Hilary J. Vernon:** Formal analysis. **Oliver Fiehn:** Writing – review & editing, Writing – original draft, Supervision, Resources, Project administration, Methodology, Investigation, Funding acquisition. **M. Roselle Abraham:** Writing – review & editing, Writing – original draft, Validation, Supervision, Resources, Project administration, Methodology, Investigation, Funding acquisition, Formal analysis, Conceptualization.

Declaration of competing interest

The authors declare that they have no known competing financial interests or personal relationships that could have appeared to influence the work reported in this paper.

Data availability

Raw files and unprocessed mass spectrometry data are available at the National Metabolomics Data Repository (Metabolomics Workbench). The databased entry IDs are ST002801 (GC-TOF), ST002815 (HILIC), and ST002817 (Lipidomics). The Sequence Read Archive (SRA) accession number for the mRNA-seq library reported here is SRP083078.

Acknowledgements

This work was supported by funding from the Department of Defense (PR171587 to MRA), West Coast Metabolomics Center Pilot Award (NIH U2C ES030158), Spieker Foundation (to MRA), National Institutes of Health (R00-HL-141702 to AK, R35GM145352 to RF), the Leukemia Research Foundation (Grant#941997 to AK) and Cedars-Sinai Cancer through the 2023 Cancer Biology Program Developmental Funds Award (A.K.) and the 2022 Cancer Biology Program Cardio-Oncology Award (A.K.). The content is solely the responsibility of the authors and does not necessarily reflect the official views of the National Institute of Health. We are grateful to Dr. Gabriela V. Greenland for assistance with colony management, and Dr. Junaid Afzal for assistance with sample preparation.

Appendix A. Supplementary data

Supplementary data to this article can be found online at https://doi.org/10.1016/j.jmccpl.2024.100073.

References

[1] Maron BJ, Maron MS, Semsarian C. Genetics of hypertrophic cardiomyopathy after 20 years: clinical perspectives. J. Am. Coll. Cardiol. 2012;60(8):705–15.
[2] Spudich JA. Three perspectives on the molecular basis of hypercontractility caused by hypertrophic cardiomyopathy mutations. Pflugers Arch. 2019;471(5):701–17.

[3] Sequeira V, Najafi A, McConnell M, Fowler ED, Bollen IA, Wust RC, et al. Synergistic role of ADP and Ca(2+) in diastolic myocardial stiffness. J. Physiol. 2015;593(17):3899–916.
[4] Arad M, Seidman JG, Seidman CE. Phenotypic diversity in hypertrophic cardiomyopathy. Hum. Mol. Genet. 2002;11(20):2499–506.
[5] Robinson P, Liu X, Sparrow A, Patel S, Zhang YH, Casadei B, et al. Hypertrophic cardiomyopathy mutations increase myofilament Ca(2+) buffering, alter intracellular Ca(2+) handling, and stimulate Ca(2+)-dependent signaling. J. Biol. Chem. 2018;293(27):10487–99.
[6] Schober T, Huke S, Venkataraman R, Gryshchenko O, Kryshtal D, Hwang HS, et al. Myofilament Ca sensitization increases cytosolic Ca binding affinity, alters intracellular Ca homeostasis, and causes pause-dependent Ca-triggered arrhythmia. Circ. Res. 2012;111(2):170–9.
[7] Tardiff JC. Thin filament mutations: developing an integrative approach to a complex disorder. Circ. Res. 2011;108(6):765–82.
[8] Blanchard E, Seidman C, Seidman JG, LeWinter M, Maughan D. Altered crossbridge kinetics in the alphaMHC403/+ mouse model of familial hypertrophic cardiomyopathy. Circ. Res. 1999;84(4):475–83.
[9] Ertz-Berger BR, He H, Dowell C, Factor SM, Haim TE, Nunez S, et al. Changes in the chemical and dynamic properties of cardiac troponin T cause discrete cardiomyopathies in transgenic mice. Proc. Natl. Acad. Sci. USA 2005;102(50):18219–24.
[10] Witjas-Paalberends ER, Ferrara C, Scellini B, Piroddi N, Montag J, Tesi C, et al. Faster cross-bridge detachment and increased tension cost in human hypertrophic cardiomyopathy with the R403Q MYH7 mutation. J. Physiol. 2014;592(15):3257–72.
[11] Sequeira V, Wijnker PJ, Nijenkamp LL, Kuster DW, Najafi A, Witjas-Paalberends ER, et al. Perturbed length-dependent activation in human hypertrophic cardiomyopathy with missense sarcomeric gene mutations. Circ. Res. 2013;112(11):1491–505.
[12] Hassoun R, Budde H, Zhazykbayeva S, Herwig M, Sieme M, Delalat S, et al. Stress activated signalling impaired protein quality control pathways in human hypertrophic cardiomyopathy. Int. J. Cardiol. 2021;344:160–9.
[13] Vakrou S, Fukunaga R, Foster DB, Sorensen L, Liu Y, Guan Y, et al. Allele-specific differences in transcriptome, miRNome, and mitochondrial function in two hypertrophic cardiomyopathy mouse models. JCI Insight 2018;3(6).
[14] Vakrou S, Liu Y, Zhu L, Greenland GV, Simsek B, Hebl VB, et al. Differences in molecular phenotype in mouse and human hypertrophic cardiomyopathy. Sci. Rep. 2021;11(1):13163.
[15] Ingwall JS. The energetic cost of contraction is higher in the myocardium of patients with hypertrophic cardiomyopathy. Cardiovasc. Res. 2014;103(2):192–3.
[16] Ashrafian H, Redwood C, Blair E, Watkins H. Hypertrophic cardiomyopathy: a paradigm for myocardial energy depletion. Trends Genet. 2003;19(5):263–8.
[17] Vakrou S, Abraham MR. Hypertrophic cardiomyopathy: a heart in need of an energy bar? Front. Physiol. 2014;5:309.
[18] van der Velden J, Tocchetti CG, Varricchi G, Bianco A, Sequeira V, Hilfiker-Kleiner D, et al. Metabolic changes in hypertrophic cardiomyopathies: scientific update from the Working Group of Myocardial Function of the European Society of Cardiology. Cardiovasc. Res. 2018;114(10):1273–80.
[19] Ritterhoff J, Young S, Villet O, Shao D, Neto FC, Bettcher LF, et al. Metabolic remodeling promotes cardiac hypertrophy by directing glucose to aspartate biosynthesis. Circ. Res. 2020;126(2):182–96.
[20] Tran DH, Wang ZV. Glucose metabolism in cardiac hypertrophy and heart failure. J. Am. Heart Assoc. 2019;8(12):e012673.
[21] Hill BG. A metabocentric view of cardiac remodeling. Curr Opin Physio 2019;10:43–8.
[22] Tardiff JC, Carrier L, Bers DM, Poggesi C, Ferrantini C, Coppini R, et al. Targets for therapy in sarcomeric cardiomyopathies. Cardiovasc. Res. 2015;105(4):457–70.
[23] O. Fiehn, Metabolomics by gas chromatography-mass spectrometry: combined targeted and untargeted profiling, Curr Protoc Mol Biol 114 (2016) 30 4 1–30 4 32.
[24] Fiehn O. Metabolomics—the link between genotypes and phenotypes. Plant Mol. Biol. 2002;48(1–2):155–71.
[25] Fiehn O, Kind T. Metabolite profiling in blood plasma. Methods Mol. Biol. 2007;358:3–17.
[26] Tsugawa H, Cajka T, Kind T, Ma Y, Higgins B, Ikeda K, et al. MS-DIAL: data-independent MS/MS deconvolution for comprehensive metabolome analysis. Nat. Methods 2015;12(6):523–6.
[27] Previs MJ, O'Leary TS, Morley MP, Palmer BM, LeWinter M, Yob JM, et al. Defects in the proteome and metabolome in human hypertrophic cardiomyopathy. Circ. Heart Fail. 2022;15(6):e009521.
[28] Ranjbarvaziri S, Kooiker KB, Ellenberger M, Fajardo G, Zhao M, Vander Roest AS, et al. Altered cardiac energetics and mitochondrial dysfunction in hypertrophic cardiomyopathy. Circulation 2021;144(21):1714–31.
[29] Wang W, Wang J, Yao K, Wang S, Nie M, Zhao Y, et al. Metabolic characterization of hypertrophic cardiomyopathy in human heart. Nature Cardiovascular Research 2022;1(5):445–61.
[30] Karlstadt A, Fliegner D, Kararigas G, Ruderisch HS, Regitz-Zagrosek V, Holzhutter HG. CardioNet: a human metabolic network suited for the study of cardiomyocyte metabolism. BMC Syst. Biol. 2012;6:114.
[31] He H, Javadpour MM, Latif F, Tardiff JC, Ingwall JS. R-92L and R-92W mutations in cardiac troponin T lead to distinct energetic phenotypes in intact mouse hearts. Biophys. J. 2007;93(5):1834–44.
[32] Vikstrom KL, Factor SM, Leinwand LA. Mice expressing mutant myosin heavy chains are a model for familial hypertrophic cardiomyopathy. Mol. Med. 1996;2(5):556–67.
[33] Moolman JC, Corfield VA, Posen B, Ngumbela K, Seidman C, Brink PA, et al. Sudden death due to troponin T mutations. J. Am. Coll. Cardiol. 1997;29(3):549–55.
[34] Abraham MR, Bottomley PA, Dimaano VL, Pinheiro A, Steinberg A, Traill TA, et al. Creatine kinase adenosine triphosphate and phosphocreatine energy supply in a single kindred of patients with hypertrophic cardiomyopathy. Am. J. Cardiol. 2013;112(6):861–6.
[35] Geisterfer-Lowrance AA, Kass S, Tanigawa G, Vosberg HP, McKenna W, Seidman CE, et al. A molecular basis for familial hypertrophic cardiomyopathy: a beta cardiac myosin heavy chain gene missense mutation. Cell 1990;62(5):999–1006.
[36] Volkmann N, Lui H, Hazelwood L, Trybus KM, Lowey S, Hanein D. The R403Q myosin mutation implicated in familial hypertrophic cardiomyopathy causes disorder at the actomyosin interface. PLoS One 2007;2(11):e1123.
[37] Becker KD, Gottshall KR, Hickey R, Perriard JC, Chien KR. Point mutations in human beta cardiac myosin heavy chain have differential effects on sarcomeric structure and assembly: an ATP binding site change disrupts both thick and thin filaments, whereas hypertrophic cardiomyopathy mutations display normal assembly. J. Cell Biol. 1997;137(1):131–40.
[38] Crilley JG, Boehm EA, Blair E, Rajagopalan B, Blamire AM, Styles P, et al. Hypertrophic cardiomyopathy due to sarcomeric gene mutations is characterized by impaired energy metabolism irrespective of the degree of hypertrophy. J. Am. Coll. Cardiol. 2003;41(10):1776–82.
[39] Kawana M, Spudich JA, Ruppel KM. Hypertrophic cardiomyopathy: mutations to mechanisms to therapies. Front. Physiol. 2022;13:975076.
[40] Guinto PJ, Haim TE, Dowell-Martino CC, Sibinga N, Tardiff JC. Temporal and mutation-specific alterations in Ca2+ homeostasis differentially determine the progression of cTnT-related cardiomyopathies in murine models. Am. J. Physiol. Heart Circ. Physiol. 2009;297(2):H614–26.
[41] Chandra M, Tschirgi ML, Tardiff JC. Increase in tension-dependent ATP consumption induced by cardiac troponin T mutation. Am. J. Physiol. Heart Circ. Physiol. 2005;289(5):H2112–9.
[42] Colegrave M, Peckham M. Structural implications of beta-cardiac myosin heavy chain mutations in human disease. Anat Rec (Hoboken) 2014;297(9):1670–80.
[43] Lowey S, Bretton V, Joel PB, Trybus KM, Gulick J, Robbins J, et al. Hypertrophic cardiomyopathy R403Q mutation in rabbit beta-myosin reduces contractile function at the molecular and myofibrillar levels. Proc. Natl. Acad. Sci. USA 2018;115(44):11238–43.
[44] Fatkin D, McConnell BK, Mudd JO, Semsarian C, Moskowitz IG, Schoen FJ, et al. An abnormal Ca(2+) response in mutant sarcomere protein-mediated familial hypertrophic cardiomyopathy. J. Clin. Invest. 2000;106(11):1351–9.
[45] Geisterfer-Lowrance AA, Christe M, Conner DA, Ingwall JS, Schoen FJ, Seidman CE, et al. A mouse model of familial hypertrophic cardiomyopathy. Science 1996;272(5262):731–4.
[46] Cannon L, Yu ZY, Marciniec T, Waardenberg AJ, Iismaa SE, Nikolova-Krstevski V, et al. Irreversible triggers for hypertrophic cardiomyopathy are established in the early postnatal period. J. Am. Coll. Cardiol. 2015;65(6):560–9.
[47] Tardiff JC, Hewett TE, Palmer BM, Olsson C, Factor SM, Moore RL, et al. Cardiac troponin T mutations result in allele-specific phenotypes in a mouse model for hypertrophic cardiomyopathy. J. Clin. Invest. 1999;104(4):469–81.
[48] Zacchigna S, Paldino A, Falcao-Pires I, Daskalopoulos EP, Dal Ferro M, Vodret S, et al. Towards standardization of echocardiography for the evaluation of left ventricular function in adult rodents: a position paper of the ESC Working Group on Myocardial Function. Cardiovasc. Res. 2021;117(1):43–59.
[49] Matyash V, Liebisch G, Kurzchalia TV, Shevchenko A, Schwudke D. Lipid extraction by methyl-tert-butyl ether for high-throughput lipidomics. J. Lipid Res. 2008;49(5):1137–46.
[50] Kind T, Wohlgemuth G, Lee DY, Lu Y, Palazoglu M, Shahbaz S, et al. FiehnLib: mass spectral and retention index libraries for metabolomics based on quadrupole and time-of-flight gas chromatography/mass spectrometry. Anal. Chem. 2009;81(24):10038–48.
[51] Skogerson K, Wohlgemuth G, Barupal DK, Fiehn O. The volatile compound BinBase mass spectral database. BMC Bioinformatics 2011;12:321.
[52] Aksentijevic D, McAndrew DJ, Karlstadt A, Zervou S, Sebag-Montefiore L, Cross R, et al. Cardiac dysfunction and peri-weaning mortality in malonyl-coenzyme A decarboxylase (MCD) knockout mice as a consequence of restricting substrate plasticity. J. Mol. Cell. Cardiol. 2014;75:76–87.
[53] Karlstaedt A, Zhang X, Vitrac H, Harmancey R, Vasquez H, Wang JH, et al. Oncometabolite d-2-hydroxyglutarate impairs alpha-ketoglutarate dehydrogenase and contractile function in rodent heart. Proc. Natl. Acad. Sci. USA 2016;113(37):10436–41.
[54] Ch'en FF, Vaughan-Jones RD, Clarke K, Noble D. Modelling myocardial ischaemia and reperfusion. Prog. Biophys. Mol. Biol. 1998;69(2–3):515–38.
[55] Cortassa S, Aon MA, O'Rourke B, Jacques R, Tseng HJ, Marban E, et al. A computational model integrating electrophysiology, contraction, and mitochondrial bioenergetics in the ventricular myocyte. Biophys. J. 2006;91(4):1564–89.
[56] Chua BH, Siehl DL, Morgan HE. A role for leucine in regulation of protein turnover in working rat hearts. Am. J. Phys. 1980;239(6):E510–4.
[57] Goodwin GW, Ahmad F, Doenst T, Taegtmeyer H. Energy provision from glycogen, glucose, and fatty acids on adrenergic stimulation of isolated working rat hearts. Am. J. Phys. 1998;274(4 Pt 2):H1239–47.
[58] Swanton EM, Saggerson ED. Effects of adrenaline on triacylglycerol synthesis and turnover in ventricular myocytes from adult rats. Biochem. J. 1997;328(Pt 3):913–22.

[59] Karlstädt A, Fliegner D, Kararigas G, Ruderisch HS, Regitz-Zagrosek V, H.-G.. Holzhütter, CardioNet: a human metabolic network suited for the study of cardiomyocyte metabolism. BMC Syst. Biol. 2012;6:114.
[60] Gurobi L. Optimization, Gurobi Optimizer Reference Manual. 2021.
[61] Ogata H, Goto S, Sato K, Fujibuchi W, Bono H, Kanehisa M. KEGG: Kyoto Encyclopedia of Genes and Genomes. Nucleic Acids Res. 1999;27(1):29–34.
[62] Benjamini Y, Drai D, Elmer G, Kafkafi N, Golani I. Controlling the false discovery rate in behavior genetics research. Behav. Brain Res. 2001;125(1–2):279–84.
[63] Barupal DK, Fiehn O. Chemical Similarity Enrichment Analysis (ChemRICH) as alternative to biochemical pathway mapping for metabolomic datasets. Sci. Rep. 2017;7(1):14567.
[64] Liu Y, Afzal J, Vakrou S, Greenland GV, Talbot Jr CC, Hebl VB, et al. Differences in microRNA-29 and pro-fibrotic gene expression in mouse and human hypertrophic cardiomyopathy. Front Cardiovasc Med 2019;6:170.
[65] Olsson MC, Palmer BM, Leinwand LA, Moore RL. Gender and aging in a transgenic mouse model of hypertrophic cardiomyopathy. Am. J. Physiol. Heart Circ. Physiol. 2001;280(3):H1136–44.
[66] Spindler M, Saupe KW, Christe ME, Sweeney HL, Seidman CE, Seidman JG, et al. Diastolic dysfunction and altered energetics in the alphaMHC403/+ mouse model of familial hypertrophic cardiomyopathy. J. Clin. Invest. 1998;101(8):1775–83.
[67] Gillespie M, Jassal B, Stephan R, Milacic M, Rothfels K, Senff-Ribeiro A, et al. The reactome pathway knowledgebase 2022. Nucleic Acids Res. 2022;50(D1): D687–92.
[68] Edgar R, Domrachev M, Lash AE. Gene Expression Omnibus: NCBI gene expression and hybridization array data repository. Nucleic Acids Res. 2002;30(1):207–10.
[69] Barrett T, Wilhite SE, Ledoux P, Evangelista C, Kim IF, Tomashevsky M, et al. NCBI GEO: archive for functional genomics data sets—update. Nucleic Acids Res. 2013; 41(Database issue):D991–5.
[70] Aksentijevic D, Karlstaedt A, Basalay MV, O'Brien BA, Sanchez-Tatay D, Eminaga S, et al. Intracellular sodium elevation reprograms cardiac metabolism. Nat. Commun. 2020;11(1):4337.
[71] McClements L, Richards C, Patel N, Chen H, Sesperez K, Bubb KJ, et al. Impact of reduced uterine perfusion pressure model of preeclampsia on metabolism of placenta, maternal and fetal hearts. Sci. Rep. 2022;12(1):1111.
[72] Lu DY, Pozios I, Haileselassie B, Ventoulis I, Liu H, Sorensen LL, et al. Clinical outcomes in patients with nonobstructive, labile, and obstructive hypertrophic cardiomyopathy. J. Am. Heart Assoc. 2018;7(5).
[73] Sivalokanathan S, Zghaib T, Greenland GV, Vasquez N, Kudchadkar SM, Kontari E, et al. Hypertrophic cardiomyopathy patients with paroxysmal atrial fibrillation have a high burden of left atrial fibrosis by cardiac magnetic resonance imaging. JACC Clin Electrophysiol 2019;5(3):364–75.
[74] Vasquez N, Ostrander BT, Lu DY, Ventoulis I, Haileselassie B, Goyal S, et al. Low left atrial strain is associated with adverse outcomes in hypertrophic cardiomyopathy patients. J. Am. Soc. Echocardiogr. 2019;32(5):593–603 e1.
[75] Karlstaedt A, Khanna R, Thangam M, Taegtmeyer H. Glucose 6-phosphate accumulates via phosphoglucose isomerase inhibition in heart muscle. Circ. Res. 2020;126(1):60–74.
[76] Watkins H, McKenna WJ, Thierfelder L, Suk HJ, Anan R, O'Donoghue A, et al. Mutations in the genes for cardiac troponin T and alpha-tropomyosin in hypertrophic cardiomyopathy. N. Engl. J. Med. 1995;332(16):1058–64.
[77] Daum G. Lipids of mitochondria. Biochim. Biophys. Acta 1985;822(1):1–42.
[78] Oemer G, Koch J, Wohlfarter Y, Alam MT, Lackner K, Sailer S, et al. Phospholipid acyl chain diversity controls the tissue-specific assembly of mitochondrial cardiolipins. Cell Rep. 2020;30(12):4281–4291 e4.
[79] Bertero E, Kutschka I, Maack C, Dudek J. Cardiolipin remodeling in Barth syndrome and other hereditary cardiomyopathies. Biochim. Biophys. Acta Mol. basis Dis. 2020;1866(8):165803.
[80] Harayama T, Riezman H. Understanding the diversity of membrane lipid composition. Nat. Rev. Mol. Cell Biol. 2018;19(5):281–96.
[81] Paredes A, Justo-Mendez R, Jimenez-Blasco D, Nunez V, Calero I, Villalba-Orero M, et al. Gamma-linolenic acid in maternal milk drives cardiac metabolic maturation. Nature 2023;618(7964):365–73.
[82] Huke S, Venkataraman R, Faggioni M, Bennuri S, Hwang HS, Baudenbacher F, et al. Focal energy deprivation underlies arrhythmia susceptibility in mice with calcium-sensitized myofilaments. Circ. Res. 2013;112(10):1334–44.
[83] Zhou L, Solhjoo S, Millare B, Plank G, Abraham MR, Cortassa S, et al. Effects of regional mitochondrial depolarization on electrical propagation: implications for arrhythmogenesis. Circ. Arrhythm. Electrophysiol. 2014;7(1):143–51.
[84] Kataoka A, Hemmer C, Chase PB. Computational simulation of hypertrophic cardiomyopathy mutations in troponin I: influence of increased myofilament calcium sensitivity on isometric force, ATPase and [Ca2+]i. J. Biomech. 2007;40 (9):2044–52.
[85] Semsarian C, Ahmad I, Giewat M, Georgakopoulos D, Schmitt JP, McConnell BK, et al. The L-type calcium channel inhibitor diltiazem prevents cardiomyopathy in a mouse model. J. Clin. Invest. 2002;109(8):1013–20.
[86] Said SM, Dearani JA, Ommen SR, Schaff HV. Surgical treatment of hypertrophic cardiomyopathy. Expert. Rev. Cardiovasc. Ther. 2013;11(5):617–27.
[87] Braunwald E, Saberi S, Abraham TP, Elliott PM, Olivotto I. Mavacamten: a first-in-class myosin inhibitor for obstructive hypertrophic cardiomyopathy. Eur. Heart J. 2023;44(44):4622–33.
[88] Ralph-Edwards A, Vanderlaan RD, Bajona P. Transaortic septal myectomy: techniques and pitfalls. Ann Cardiothorac Surg 2017;6(4):410–5.
[89] Larson PEZ, Tang S, Liu X, Sinha A, Dwork N, Sivalokanathan S, et al. Regional quantification of cardiac metabolism with hyperpolarized [1-(13)C]-pyruvate CMR evaluated in an oral glucose challenge. J. Cardiovasc. Magn. Reson. 2023;25(1):77.
[90] Schuldt M, van Driel B, Algul S, Parbhudayal RY, Barge-Schaapveld D, Guclu A, et al. Distinct metabolomic signatures in preclinical and obstructive hypertrophic cardiomyopathy. Cells 2021;10(11).
[91] Tilo Thottakara CSL, Padmanabhan Arun, Olgin Jeffrey, Roselle Abraham M. Molecular insights into the phenotypic heterogeneity observed in two different murine models of hypertrophic cardiomyopathy (HCM). Circ. Res. 2023;133: AP1141.